Review

Optical properties and biomedical applications of plasmonic nanoparticles

Nikolai G. Khlebtsov [a,b,*], Lev A. Dykman [a]

[a] Institute of Biochemistry and Physiology of Plants and Microorganisms, RAS, 13 Pr. Entuziastov, Saratov 410049, Russian Federation
[b] Saratov State University, 83 Ul. Astrakhanskaya, Saratov 410012, Russian Federation

ABSTRACT

Nanoparticle plasmonics is a rapidly emerging research field that deals with the fabrication and optical characterization of noble metal nanoparticles of various size, shape, structure, and tunable plasmon resonances over VIS-NIR spectral band. The recent simultaneous advances in synthesis, characterization, electromagnetic simulation, and surface functionalization of plasmonic nanoparticles by biospecific molecular probes have led to a perfect publication storm in discoveries and potential biomedical applications of plasmon-resonant nanoparticle bioconjugates. Here, we present an overview of these topics. First, we discus basic wet-chemical routes to fabricate conjugates of gold, silver, or composite particles with controllable size, shape, structure and with surface functionalization by biospecific molecules. Second, we consider the single-particle dipole and multipole optics and coupled plasmonic nanoparticle arrays. Finally, we discus application of plasmonic bioconjugates to such fields as homogeneous and solid-phase assays, biomedical sensing and imaging, biodistribution and toxicity aspects, drug delivery and plasmonic photothermal therapy.

© 2009 Published by Elsevier Ltd.

Contents

* Corresponding author at: Institute of Biochemistry and Physiology of Plants and Microorganisms, RAS, 13 Pr. Entuziastov, Saratov 410049, Russian Federation. Tel.: +7 8452 970 403; fax: +7 8452 970 383.
E-mail address: khlebtsov@ibppm.sgu.ru (N.G. Khlebtsov).

1. Introduction

The metal (mainly gold) nanoparticles (NPs) [1,2] have attracted significant interest as a novel platform for nanobiotechnology and biomedicine [3,4] because of convenient surface bioconjugation with molecular probes and remarkable optical properties related with the localized plasmon resonance (PR) [5]. Recently published examples include applications of NPs to genomics [6], biosensorics [7], immunoassays [8], clinical chemistry [9], detection and control of microorganisms [10], cancer cell photothermolysis [11,12], targeted delivery of drugs or other substances [13], optical imaging and monitoring of biological cells and tissues by exploiting resonance scattering [14], optical coherence tomography [15], two-photon luminescence [16], or photoacoustic [17] techniques. One of outstanding examples is rapid development of methamaterials with the optical negative refractive index [18].

Simultaneous advances in *making, measuring, and modeling* plasmonic NPs (designated as the 3M's principle [19]) have led to a perfect publication storm in discoveries and potential applications of plasmon-resonant NPs bioconjugates. At present, one can point to several trends in the recent development of physical [20] and biomedical [21] plasmonics. First, the rapid progress in convenient technologies of gold [22,23] and silver [24] NPs synthesis has provided wide possibilities for researchers, beginning from the commonly known colloidal gold nanospheres, nanorods, or silica/gold nanoshells, and ending by exotic structures such as nanocubes [25], nanorice [26], nanostars [27], or nanocages [28]. Furthermore, the development electron-beam-lithography [29] or "nanosphere lithography" [30] technologies allows fabrication of various nanostructures with fully controlled spatial parameters. Second, the computer simulations of the electromagnetic properties have been expanded from simple and small single-particle scatterers to more complex single-particle or multiparticle structures [31,32]. Third, the traditional characterization methods such as TEM and absorption spectroscopy of colloids have been greatly improved by taking advantage of single-particle technologies. In particular, these techniques are based on the resonance scattering dark-filed spectroscopy [33], the absorption of individual particles [34] (the spatial-mod-

ulation spectroscopy [35]) or their surrounding (the photothermal heterodyne imaging method) [36,37], and on the near-filed optical microscopy [38]. Finally, the development of robust surface functionalization protocols [39–41] have stimulated numerous biomedical applications of plasmon-resonant bioconjugates with various probing molecules including DNA oligonucleotides, poly- and monoclonal antibodies (Ab), streptavidin, enzymes, etc.

Here, we present a short discussion of the above trends. Keeping in mind the limitations of the review volume and an enormous volume of the literature data, we avoid any detailed discussion and citation. For the most updated information, the readers are referred to several recent reviews discussing the particle fabrication, functionalization, and optical characterization [20–24,31,32,35,39–53] as well as analytical and biomedical applications [1,2,7,9–13,54–66].

2. Chemical wet synthesis and functionalization of plasmon-resonant NPs

2.1. Nanosphere colloids (CG)

Perhaps, colloidal gold is the first nanomaterial, which history goes back to 5th or 4th century B.C. in Egypt and China (see, e.g., reviews [1,22]). The actual scientific study of CG was pioneered by Faraday [67], Zsigmondy [68], Mie [69], and Svedberg [70]. At present, the most popular colloidal synthesis protocols involve the reduction of HAuCl$_4$ (tetrachloroauric acid, TCCA) by various reducing agents. In 1951, Turkevich et al. [71] introduced very convenient citrate method, which was further developed by Frens [72] to produce relatively monodisperse particles with the controlled average equivolume diameter from 10 to 60 nm. Fabrication of smaller particles can be achieved by using sodium borohydride, a mixture of borohydride with EDTA [73] (5 nm) or sodium or potassium thiocyanate [74] (1–2 nm). For particles larger than 20 nm, the citrate method gives elongated particles [73,75]. To improve the particle shape of large particles, several approaches were suggested [1,76]. The relevant references and discussion can be found in [22,23]. Recent advances

and challenges in the silver particle fabrication have been considered in review [24] and paper [77].

2.2. Metal nanorods

PR of gold nanorods (NRs) can be easily tuned over 650–1500 nm by simple variation in the NR length or aspect ratio. Historically, the first fabrication of gold NRs was performed by using hard-template method (electrochemical deposition in a porous membrane) [78]. Perhaps, Wang et al. [79] were first who introduced a combination of surfactant additives and an electrochemical oxidation/reduction procedure to prepare colloidal gold NRs with the average thickness of about 10 nm and the aspect ratio ranging from 1.5 to 11. At present, the most popular is a two-step seed-mediated CTAB-assisted protocol suggested by Murphy [80] and El-Sayed [81] groups (CTAB = cetyltrimethylammonium bromide). In step 1, seed gold particles are formed by adding aqueous sodium borohydride to a mixed aqueous solution of CTAB and TCAA. In step 2, gold NRs are grown by adding the gold seeds to a growth solution containing CTAB, silver nitrate, TCAA, and ascorbic acid. Usually, the NRs are allowed to grow overnight without stirring.

To improve the quality of as prepared samples, one can use the separation in a glycerol concentration gradient as described in Ref. [82] (Fig. 1). Quite recently, Sharma et al. [83] described the use of a simple centrifugation approach for efficient separation of colloidal gold nanorods from a mixture of nanorods and nanospheres. For high-aspect ratio NRs, Khanal and Zubarev [84] described another approach that relies on the partial dissolution of byproduct particles with Au(III)/CTAB complex. Because of the reduction in size, the impurities become fully soluble in water and can be separated from NRs. A summary of recent advantages in gold NRs synthesis can be found in reviews [85–87] and papers [88,89].

Gold NRs can be used as templates for deposition of a thin silver layer [90] through the reduction of silver nitrate by ascorbic acid in a presence of CTAB, polyvinyl pyrrolidone, and NaOH to rise pH [91,92]. Such bimetal

Au–Ag particles can conveniently be tuned from NIR to VIS through the increase in silver layer.

2.3. Metal nanoshells

Silica (core)/gold (shell) particles present an example of NPs with PR that can be tuned over 600–1500 nm by variation in the particle structure, i.e. in their ratio shell thickness/core radius. In 1998, Halas et al. [93] developed a two-step protocol involving fabrication of silica nanospheres followed by their amination, attachment of fine (2–4 nm) gold seeds, and formation of a complete gold shell by reducing of TCCA on seeds. A summary of 10-year development of this approach is given in Ref. [94]. Phonthammachai et al. suggested a one-step modification of the Halas method [95], whereas Prasad et al. described a method for synthesis of polystyrene sphere/gold nanoshells [96]. Fabrication of silver and gold–silver alloy nanoshells (NSs) on silica cores has been described in several publications [97,98]. By using silica/gold or gold/silica/gold NSs as precursors, Ye et al. [99] developed a versatile method to fabricate hollow gold nanobowls and complex nanobowls (with a gold core) based on an ion milling and a vapor HF etching technique. Such a NPs being assembled on a substrate can be considered as promise SERS platform for biomolecular detection. Xia et al. introduced a new protocol based on galvanic replacement of silver ions by reducing gold atoms [100,101]. This approach allows to produce a variety of particle shapes and structures, beginning from silver cubes (polyol process [102]) and ending by nanocages [103]. Formation of such particles is accompanied by red-shifting of PR from 400 to 1000 nm.

2.4. Other particles and NP assemblies

To date, one can find a lot of published protocols for fabrication of NPs with various shapes and structure. In particular, the reducing of TCCA on 10–15 nm gold seed leads to formation of gold nanostars [27], while the using
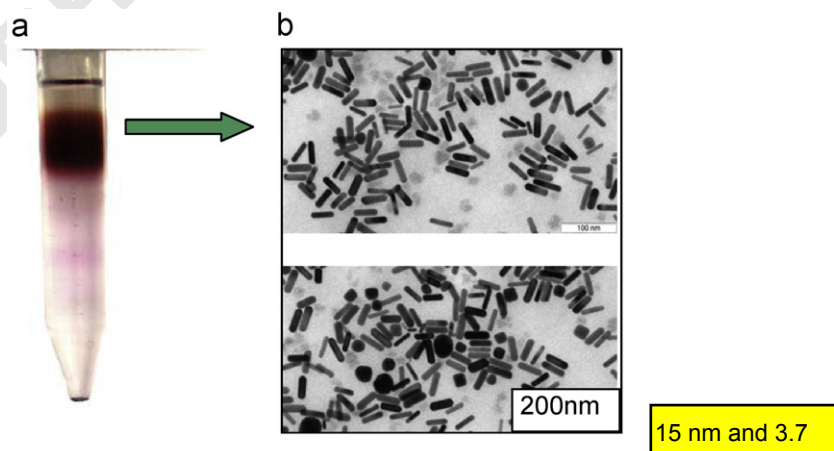

Fig. 1. (a) Separation of a NR sample in a stepwise glycerol gradient. The particle diameter and the aspect ratio are 15 and 3.7 nm, respectively; the longitudinal resonance wavelength equals 780 nm. (b) TEM image of the upper portion of the first major fraction from the separation tube (top) and as prepared sample before separation (bottom).

of multiple twinned seeds produced gold bipyramids [104]. A combination of ethylene glycol with PDDA cationic surfactant was shown to be an effective polyol route for the controllable synthesis of high-quality gold octahedral [105].

Apart from fabrication of isolated NPs, it is also very important to assembly NPs into 1D-, 2D-, and 3D-structures. The ultimate goal of this approach is to explore the collective physical properties of the assemblies, which are different from those of isolated NPs. To this end, various strategies (solvent evaporation, electrostatic attraction, hydrogen bonding, DNA-driven assembly, and cross-linking induced by biospecific interaction like antigen–antibody and so on) have been developed to form NP assemblies and utilize them in the fabrication of nanostructured devices [39].

Although semiconductor quantum dots (QDs) have attracted significant interest because of small size and extra high fluorescence quantum yield [47], their toxicity limits possibly biomedical applications. In 2003, Dickson et al. [106] reported successful fabrication of water-soluble Au_8 nanodots embedded in poly(amidoamine) (PMAM) dendrimers. Such nanostructures showed strong size-specific 450 nm emission at 384 nm irradiation with

very high (about 40%) quantum yield, in contrast to previous observations for low-effective Au QDs [107].

Because of volume limitations, we have to restrict ourselves by indicating the above (and other not cited!) recent reviews. Accordingly, this review should be considered as a starting point for further reading. In conclusion, we show a gallery of particles mentioned in this section (Fig. 2).

3. Optical properties

3.1. Basic physical principles

Collective excitations of conductive electrons in metals are called "plasmons" [5]. Depending on the boundary conditions, it is commonly accepted to distinguish bulk plasmons (3D plasma), surface propagating plasmons or surface plasmon polaritons (2D films), and surface localized plasmons (nanoparticles) (Fig. 3). A quantum of bulk plasmons $\hbar\omega_p$ is about 10 eV for noble metals. Because of longitudinal nature, the bulk plasmons cannot be excited by visible light. The surface plasmon polaritons propagate along metal surfaces in a waveguide-like fashion. Below, we shall consider only the nanoparticle
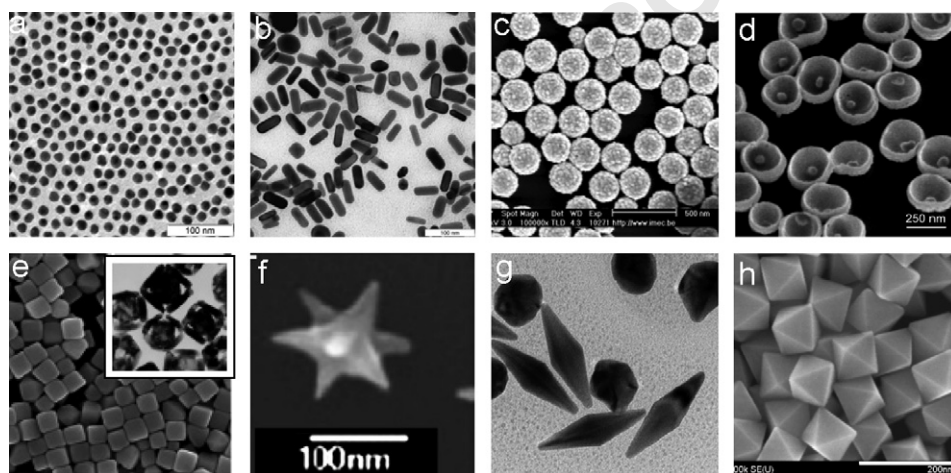
Fig. 2. TEM images of 15 nm colloidal gold (a), 15 × 50 nm gold nanorods (b), 160(core)/17(shell) nm silica/gold nanoshells (c, SEM), 250 nm Au nanobowls with 55 Au seed inside (d), silver cubes and gold nanocages (insert) (e), nanostars (f), bipyramids (g), and octahedral (h). Images (d–h) are adapted from Refs. [27,99,103–105], respectively.

Refs. [99, 103, 27, 104], and [105], respectively.
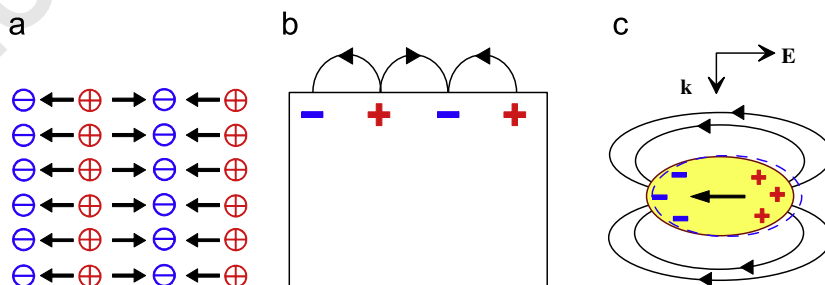
Fig. 3. Schematic representation of the bulk (a), surface propagating (b), and surface localized (c) plasmons. The dashed line shows the electron cloud displacement.

localized plasmons. In this case, the electric component of an external optical field exerts a force on the conductive electrons and displaces them from their equilibrium positions to create uncompensated charges at the nanoparticle surface (Fig. 3c). As the main effect producing the restoring force is the polarization of the particle surface, these oscillations are called "surface" plasmons which have a well-defined resonance frequency.

The most common physical approach to linear NP plasmonics is based on the linear local approximation

$$\mathbf{D}(\mathbf{r}, \omega) = \varepsilon(\mathbf{r}, \omega)\mathbf{E}(\mathbf{r}, \omega), \tag{1}$$

where ω is the angular frequency and the electric displacement $\mathbf{D}(\mathbf{r}, \omega)$ depends on the electric field $\mathbf{E}(\mathbf{r}, \omega)$ and on the dielectric function $\varepsilon(\mathbf{r}, \omega)$ only at the same position $\mathbf{r}$. Then, the liner optical response can be found by solving the Maxwell equations with appropriate boundary conditions. Actually, in the local approximation, the indicating of position vector in dielectric functions $\varepsilon(\mathbf{r}, \omega)$ may be omitted.

As the particle size a is decreased to the value comparable with the electron mean free path ($a \sim L_{eff}$), deviations of the phenomenological dielectric function $\varepsilon(\omega, a)$ of the particle from the bulk values $\varepsilon_b(\omega) = \varepsilon(\omega, a \gg l_e)$ can be expected. A general recipe for the inclusion of macroscopic tabulated data and size effects to the size-dependent dielectric function consists in the following [5,21]. Let $\varepsilon_b(\omega)$ be the macroscopic dielectric function, which can be found in the literature from measurements with massive samples [108]. Then, the size-dependent dielectric function of a particle is

$$\varepsilon(\omega, a) = \varepsilon_b(\omega) + \Delta\varepsilon(\omega, a), \tag{2}$$

where the correction $\Delta\varepsilon(\omega, a)$ takes into account the contribution of size-dependent scattering of electrons to the Drude part of the dielectric function described by the expression

$$\Delta\varepsilon(\omega, a) = \varepsilon_b^{Drude}(\omega) - \varepsilon_p^{Drude}(\omega, a) = \frac{\omega_p^2}{\omega(\omega + i\gamma_b)} - \frac{\omega_{p,a}^2}{\omega(\omega + i\gamma_p)}. \tag{3}$$

Here, $\gamma_b = \tau_b^{-1}$ is the volume decay constant; τ_b is the electron free path time in a massive metal; $\omega_{p,a}$ is the plasma frequency for a particle of diameter a (we assume below that $\omega_{p,a} \simeq \omega_p$);

$$\gamma_p = \tau_p^{-1} = \gamma_b + \gamma_s = \gamma_b + A_s \frac{v_F}{L_{eff}} \tag{4}$$

is the size-dependent decay constant equal to the inverse electron mean transit time $\gamma_p = \tau_p^{-1}$ in a particle; L_{eff} is the effective electron mean free path; γ_s is the size-dependent contribution to the decay constant; and A_s is a dimensionless parameter determined by the details of scattering of electrons by the particle surface [109,110] (which is often simply set equal to 1).

To solve the Maxwell equation, various analytical or numerical methods can be used. The most popular and simple analytical method is the dipole (electrostatic) approximation [111], developed in classic works by Rayleigh [112], Mie [69] and Gans [113] (actually, the Gans solution for ellipsoid had earlier been done by Rayleigh [114]). Among the many numerical methods available, the discrete dipole approximation (DDA) [115], the boundary element method (BEM) [20], the finite element and finite difference time domain methods (FEM and FDTDM) [116], the multiple multipole method (MMP) [117], and the T-matrix method [118] are most popular. For details, relevant references, and discussion of the advantages and drawbacks of various methods, the readers are referred to resent reviews [20,21,32,33] and book [118].

Understanding of the interaction of intense laser pulses with PR NPs requires going beyond linear response description. For instance, the second and third harmonic generation is widely known example [20]. Over the past decade, many transient transmission experiments [119] have been carried out to elucidate the time-dependent physics of nonlinear responses. These experiments involve an intense femto-second pump laser pulse followed by measuring the transmittance of a weaker probe laser beam. Fig. 4 shows a flowchart of the processes [20] accompanied the nonlinear particle response after irradiation with pump pulse. These experiments lead to better understanding the size-dependent dynamical effects (such as electron relaxation) and the temperature-dependent models of the particle dielectric function [20].

In some cases, an analytical approximation of the Drude type should be used instead of tabulated bulk $\varepsilon_b(\lambda)$ data. Such a situation appears, for example, in FDTDM method where one needs to calculate an integral convolution [116]. This integration could be performed analytically at each step of FDTDM only by using a few simple models for $\varepsilon(\omega)$, including the Drude formula. Specifically, there exists several sets of interpolation parameters for Johnson an Christy data [120] or other tabulated data [21], including the interpolation sets given by Oubre and Nordlander [121]: $\varepsilon_{ib} = 9.5$, $\omega_p = 8.95\,eV$,
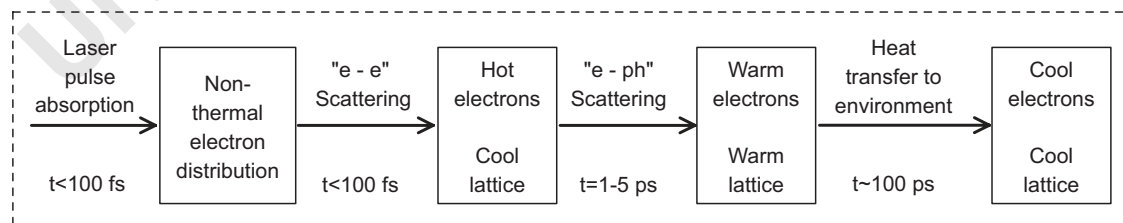

Fig. 4. Schematic of a transient NP response to absorption of a laser pulse followed by the electron–electron (e–e) and electron-phonon (e-ph) scattering and the heat exchange with environment. Adapted from [20].

$\gamma_b = 0.0691$ (gold) and $\varepsilon_{ib} = 5.0$, $\omega_p = 9.5\,\text{eV}$ and $\gamma_b = 0.0987\,\text{eV}$ (silver).

3.2. Surface-chemical and quantum-size effects

Although the basic optics of PR metal NPs can be reasonably well explained with simple models discussed in Section 3.1, there are large discrepancies between the optical properties of metal sols prepared in water, particularly those of silver, and NP ensembles prepared in other matrices. These differences can be attributed to unique double layer presented at the metal–water interface. Mulvaney in his excellent review [122] gave a thorough consideration of surface physico-chemical effects such as cathodic or anodic polarization, chemisorption, metal adatom deposition, and alloying. These processes can alter the surface plasmon absorption band of aqueous metal colloids, which is sensitive to electrochemical processes occurring at metal particle surfaces. Phenomenological description implies deviation of the surface scattering constant A_s from 1. A theoretical study to understand the origin of the increase in A_s was given by Persson [123] who considered the influence of a surface layer of adsorbed molecules on the damping rate of the localized surface plasmon. In general, the widths of the PR spectra of particles, being deposited on a substrate or embedded in a matrix, have to be interpreted with care since the net size-limiting effect may be less effective than other mechanisms and can be obscured by the chemical interface damping.

The unique properties of metal nanoparticles could help in answering the old question: "How many atoms does it take to make a solid?" Indeed, a typical metal NP can be thought as an aggregate composed of a relatively small number of atoms, starting with clusters consisting of a few atoms to large NPs with more than 10^5 atoms. Thus, these objects are intermediate in size between the domain of atoms and small molecules, which require a full quantum mechanical treatment, and the bulk materials describing by classical electrodynamics and solid-state physics. Metal NPs are the objects at mesoscopic scale between the microscopic and macroscopic worlds. So, they may exhibit a wide number of new phenomena [124], including the discrete spectrum of the electronic states and coherent motion of electrons as far as electron can propagate through the whole system without experiencing inelastic or phase-breaking scattering. In terms of quantum mechanic language, a metallic nanoparticle subject to an external driving field reveals a collective electronic excitation, the so-called surface plasmon.

The question of primary importance concerns the applicability of phenomenological modification of the Drude's. As pointed out by Kawabata and Kubo in their pioneering work [125], the interpretation of the surface plasmon line width in terms of the free path effect is "too naive, if not entirely incorrect, because in such a small particle the electron states are quantized into discrete levels which are determined by the boundary conditions at the surface." Using the linear response theory and fluctuation-dissipation theorem [125], Kawabata and Kubo arrived at the following final expression for the size-dependent contribution to the damping constant (see Eq. (4)):

$$\gamma_s = \frac{3}{4}\frac{v_F}{a}g_{kk}\left(\frac{\hbar\omega_0}{\varepsilon_F}\right) \tag{5}$$

where $g_{kk}(x)$ is a decreasing function of the surface plasmon energy $\hbar\omega_0$ normalized to the Fermi energy ε_F, and $g(0) = 1$. Surprisingly enough, the first-principle treatment has led to the same $\gamma_s \sim 1/L_{eff} \sim 1/a$ law that was established from simple physical [5] or even pure geometrical [109] approaches.

Since 1966 Kawabata and Kubo paper [125], which included significant approximations, various refinement were published (see, e.g., Refs. [5,21,126], but all these studies confirmed the same $\gamma_s \sim 1/L_{eff} \sim 1/a$ law with some minor modifications. As a matter of fact, all theoretical calculations reproduced this damping law (16), but with different parameter A_s.

In addition to the surface scattering problem, there exist other quantum effects which has been omitted in our short consideration. For example, the so-called "spill-out" effect [126] means that the electron wave function extends outside of the geometrical particle boundary resulting in a decrease of the effective electron density and in a corresponding decreasing the apparent plasma frequency. Nevertheless, the existing experimental data for noble metal NPs and the theoretical studies based on the time-dependent local density approximation for nanoshells [127] and rods [128] prove the validity of using the classical electrodynamics combined with properly size-corrected dielectric function. At this point we agree with Bohren and Huffman [111] notion that "surface modes in small particles are adequately and economically described in their essentials by simple classical theories" provided that the possible quantum effects have been included in the dielectric function.

It is also interesting to note that the plasmons in metal nanostructures exhibit some analogy to electron wave functions of simple atomic and molecular orbitals [129]. It has been recently realized that this analogy and the "plasmon hybridization" concept [130] can be exploited in the design of various nanostructures and understanding their optical properties.

Although the local approximation and frequency-dependent dielectric function give reasonable agreement between theory and experiment, the non-local effects can play an important role at small distances in the nanometer region [131]. As the first-principle quantum-mechanical calculations of the optical response [126] are only available for relatively simple systems (hundreds of noble metal atoms) and are insufficient for real nanoparticles, several compromise approximations have been developed to describe quantum-sized and non-local effects [127,131]. In particular, a specular reflection model [131] has been applied to describe the optical properties of small gold and silver spheres, bispheres, and nanoshells. It was shown that the non-local effects produce significant blue shift of PR and its broadening in comparison with the commonly accepted local approach.
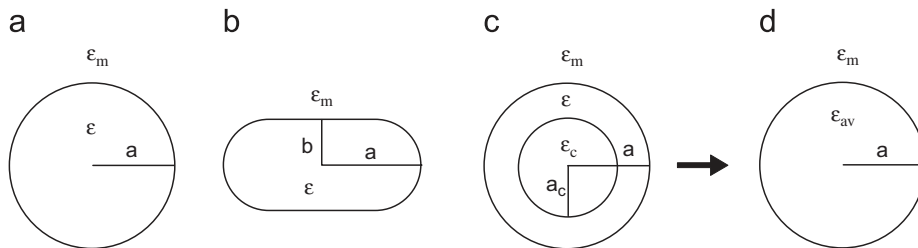
Fig. 5. Three examples of small dipole-scattering metal particles: a nanosphere of a radius a, a nanorod with semiaxes a and b (the s-cylinder model [87]), and a core-shell particle with the corresponding radii a_c and a. The dielectric functions of metal, surrounding medium, and the dielectric core are ε, ε_m, and ε_c, respectively. The core-shell particle is replaced with a homogeneous sphere of a dielectric permittivity ε_{av} according to the "dipole equivalence principle" [135].

By contrast to local relationship (1), the non-local response is described by integral convolution

$$\mathbf{D}(\mathbf{r}, \omega) = \int d\mathbf{r}' \varepsilon(\mathbf{r}', \mathbf{r}, \omega) \mathbf{E}(\mathbf{r}', \omega). \qquad (6)$$

For homogeneous media, $\varepsilon(\mathbf{r}', \mathbf{r}, \omega) = \varepsilon(|\mathbf{r}' - \mathbf{r}|, \omega)$, and after Fourier transformation we have the following momentum-space ($\mathbf{q}$) representation

$$\mathbf{D}(q, \omega) = \varepsilon(q, \omega) \mathbf{E}(q, \omega). \qquad (7)$$

The local approximation means a transition to the $q \to 0$ limit $\varepsilon(q, \omega) \to \varepsilon^{loc}(\omega)$. An approximate recipe to account for the non-local effects can be written as a modification of the above Eq. (2) [131]

$$\varepsilon(q, \omega) = \varepsilon(\omega) + \Delta\varepsilon(q, \omega) \equiv \varepsilon(\omega) + \varepsilon^{nl}(q, \omega) - \varepsilon^{Drude}(\omega), \qquad (8)$$

where $\varepsilon(\omega)$ is the experimental (local) tabulated dielectric function, $\varepsilon^{Drude}(\omega)$ is the Drude function, and $\varepsilon^{nl}(q, \omega)$ is the non-local valence-electrons response as introduced by Lindhard and Mermin [132]. With the non-local dielectric function in hand, further calculations can be made in the same fashion as with the local approximation. Several illustrative examples are presented in the above cited paper [131].

The above consideration is valid only for relatively large atom clusters. At sizes close to the Fermi wavelength of an electron, discrete nanocluster energy levels become accessible thus causing significant change in optical properties. An instructive example is Au_8 QDs described in Refs. [106,133]. Such small metal nanoclusters exhibit molecule-like transitions as the density of states is small to merge the conduction and valence bands. The luminescence from Au_8 QDs is thought to arise from electron transitions between filled "d" and "sp" conduction bands. As QDs size decreases, the level-energy spacing increases, leading to a blue shift in fluorescence relative to that from larger QDs. Therefore, in contrast to small metal NPs, Au and Ag QDs [134] demonstrate quantum mechanical behavior which cannot be treated in terms of classical electrodynamics.

3.3. Plasmon resonances

In the general case, the eigenfrequency of a "collective" plasmon oscillator does not coincide with the wave frequency and is determined by many factors, including the concentration and effective mass of conductive electrons, the shape, structure, and size of particles, interaction between particles, and the influence of the environment. However, for an elementary description of the NP optics it is sufficient to use a combination of the usual dipole (Rayleigh) approximation and the Drude theory [111]. In this case, the absorption and scattering of light by a small particle are determined by its electrostatic polarizability α, which can be calculated by using the optical dielectric function $\varepsilon(\omega)$ or $\varepsilon(\lambda)$, where λ is the wavelength of light in vacuum.

Let us consider three types of small particles shown in Fig. 5: a nanosphere of a radius a, a nanorods with semiaxes a and b, and a core-shell particle with the corresponding radii a_c and a. All the particles are assumed to have dipole-like scattering and absorption properties. The core-shell particle is replaced with a homogeneous sphere of a dielectric function ε_{av} according to the dipole equivalence principle [135].

For a small particle with an equivolume radius $a_{ev} = (3V/4\pi)^{1/3}$ embedded in a homogeneous dielectric medium with the permittivity ε_m (Fig. 5), we have the following expressions for the extinction, absorption and scattering cross sections [21]

$$C_{ext} = C_{abs} + C_{sca} = \frac{12\pi k}{a_{ev}^3} \frac{\varepsilon_m \, \mathrm{Im}(\varepsilon)}{|\varepsilon - \varepsilon_m|^2} |\alpha|^2 + \frac{8\pi}{3} k^4 |\alpha|^2 \simeq 4\pi k \, \mathrm{Im}(\alpha), \qquad (9)$$

where $k = 2\pi\sqrt{\varepsilon_m}/\lambda$ is the wave number in the surrounding medium and α is the renormalized particle polarizability [21]

$$\alpha = \frac{\alpha_0}{1 + f_{rd}(ka_v)a_{ev}^{-3}\alpha_0}, \qquad (10)$$

α_0 is the electrostatic polarizability, and the correction function $f_{rd}(ka_{ev})$ accounts for the radiative damping effects [136]. For a sphere of a radius $a_{ev} = a$ we have

$$f_{rd}(ka) = 2 + 2(ika - 1)\exp(ika) \qquad (11)$$

Below, we will not distinguish the electrostatic polarizability α_0 from the renormalized polarizability α. In this approximation $\alpha = \alpha_0$ and the extinction of a small particle is determined by its absorption $C_{abs} = C_{ext} = 4\pi k \, \mathrm{Im}(\alpha)$, whereas and scattering contribution can be neglected. For all three types of particles, the polarizability α can be written in following general form

$$\alpha = \frac{3V}{4\pi}\frac{\varepsilon - \varepsilon_m}{\varepsilon + \varphi\varepsilon_m} = \frac{3V}{4\pi}\frac{\varepsilon_{av} - \varepsilon_m}{\varepsilon_{av} + \varphi\varepsilon_m}, \tag{12}$$

where the second expression is written for the metal nanoshell and the parameter φ depends on the particle shape and structure. Specifically, $\varphi = 2$ for spheres, $\varphi = (1/L_a - 1)$ for spheroids (L_a and $L_b = (1 - L_a)/2$ are the geometrical depolarization factors [111]), and

$$\varphi = \frac{1}{2}[p_0 + (p_0^2 - (\varepsilon_c/\varepsilon_m))^{1/2}], \quad p_0 = \frac{\varepsilon_c}{\varepsilon_m}\left(\frac{3}{4f_s} - \frac{1}{2}\right) + \frac{3}{2f_s} - \frac{1}{2} \tag{13}$$

for metal nanoshells on a dielectric core [135]. Here, $f_s = (a_s/a)^3 = 1 - (a_c/a)^3$ is the volume fraction of the metal shell. For thin shells we have [135]

$$\varphi = \frac{3}{f_s}(1 + \varepsilon_c/2\varepsilon_m). \tag{14}$$

One can see from the expressions presented above that the resonance condition for polarizability and optical cross sections reads

$$\varepsilon(\omega_{max} \equiv \omega_0) = \varepsilon(\lambda_{max}) = -\varphi\varepsilon_m. \tag{15}$$

The PR frequency can be estimated from the Drude approximation for dielectric function

$$\varepsilon(\omega) = \varepsilon_{ib} - \frac{\omega_p^2}{\omega(\omega + i\gamma_b)}, \tag{16}$$

where ε_{ib} is the interband contribution, ω_p is the frequency of volume plasma oscillations of free electrons, γ_b is the volume decay constant related to the electron mean free path l_b and the Fermi velocity v_F by the expression $\gamma_b = l_b/v_F$. By combining above equations, one can obtain the following expressions for the resonance plasmon frequency and wavelength [21]

$$\omega_{max} \equiv \omega_0 = \frac{\omega_p}{\sqrt{\varepsilon_{ib} + \varphi\varepsilon_m}}, \quad \lambda_{max} \equiv \lambda_0 = \lambda_p\sqrt{\varepsilon_{ib} + \varphi\varepsilon_m}. \tag{17}$$

Here, $\lambda_p = 2\pi c/\omega_p$ is the wavelength of volume oscillations of the metal electron plasma. For gold, $\lambda_p \approx 131$ nm.

Two additional important notes are in order here. First, it follows from Eq. (17) that the dipole resonances of small gold or silver spheres ($5 \leq a \leq 20$ nm) in water is localized near 520 and 380 nm and do not depend on their size. By contrast, the dipole resonance of rods and nanoshells can be easily tuned through variation in their aspect ratio ($L_a = 1/3$(sphere)$\to$0(needle)) or the ratio shell thickness/core radius ($f_s = 1$ for a homogeneous sphere and $f_s \to 0$ for a thin shell). Second, Eq. (17) determines the very first ($n = 1$) dipole resonance of a spherical particle. In addition to the dipole resonance, higher multipoles and corresponding multipole (quadrupole, etc.) resonances can be also excited in larger particles. For each multipole mode the resonance condition exists, which is similar to Eq. (15) and corresponds to the resonance of the quadrupole, octupole, and so on contributions. For spherical particles, these conditions correspond to the resonance relations for the partial Mie coefficients [111] $\omega_n = \omega_p(\varepsilon_{ib} + \varepsilon_m(n + 1)/n)^{-1/2}$, where n is the mode (resonance) number. With an increase in the sphere size, the multipole frequency decreases [20,137].

It is important to distinguish two possible scenarios for excitation of multipole resonances. The first case corresponds to a small nonspherical particle of irregular or uneven shape, when the distribution of induced surface charges is strongly inhomogeneous and does not correspond to the dipole distribution. This inhomogeneous distribution generates high multipoles even in the case when the system size is certainly much smaller than the light wavelength. Typical examples are cubic particles [138] or two contacting spheres [139] where the field distribution near the contact point is so inhomogeneous that multipole expansions converge very slowly or diverge at all. The second scenario of high multipole excitation is realized with increasing the particle size, when the transition from the quasi-stationary to radiative regime is realized, and the contribution of higher spherical harmonics should be taken into account in the Mie series (or another multipole expansion). For example, while the extinction spectrum of a silver 30 nm NP is completely determined by the dipole contribution and has one resonance, the spectrum of a 60 nm sphere exhibits a distinct high-frequency quadrupole peak in addition to the low-frequency dipole peak.

3.4. Metal spheres

The optical properties of a small sphere are completely determined by their scattering amplitude matrix [111]. Here we are interested mainly in its extinction, absorption and scattering cross sections $C_{ext,abs,sca}$ or efficiencies $Q_{ext,abs,sca} = C_{ext,abs,sca}/S_{geom}$. From experimental point of view, we shall consider the absorbance (extinction) and the scattering intensity at a given metal concentration c

$$A_{ext} = 0.326\frac{cl}{\rho}\frac{Q_{ext}}{a_{ev}}, \quad I_{90}(\lambda, \theta_{sca}) = 0.326\frac{cl}{\rho a_{ev}}\left[\frac{16S_{11}(ka_{ev}, \theta_{sca})}{3(ka_{ev})^2}\right] \tag{18}$$

where $S_{11}(ka_{ev}, \theta)$ is the normalized intensity of scattering at an θ_{sca} angle (the first element of the Mueller scattering matrix [111]), ρ and $d = 2a$ are the metal density and the particle equivolume diameter. The expression in square brackets is normalized so that it is equal to the scattering efficiency of small particles. For metal nanoshells, Eq. (18) should be slightly modified [140].

Fig. 6 shows well known theoretical extinction and scattering spectra calculated by Mie theory for gold and silver colloids at a constant concentration of gold (57 μg/ml, corresponds to complete reduction of 0.01% HAuCl$_4$) and silver (5 μg/ml). Note that for larger particles the extinction spectra reveal quadrupole peaks and significant contribution of scattering. With an increase in the particle diameter, the spectra become red-shifted and broadened. This effect can be used for fast and convenient particle sizing [73,141,142]. The solid line in Fig. 6c shows the corresponding calibration curve based on long-term set of the literature experimental data (shown by different symbols) [141]
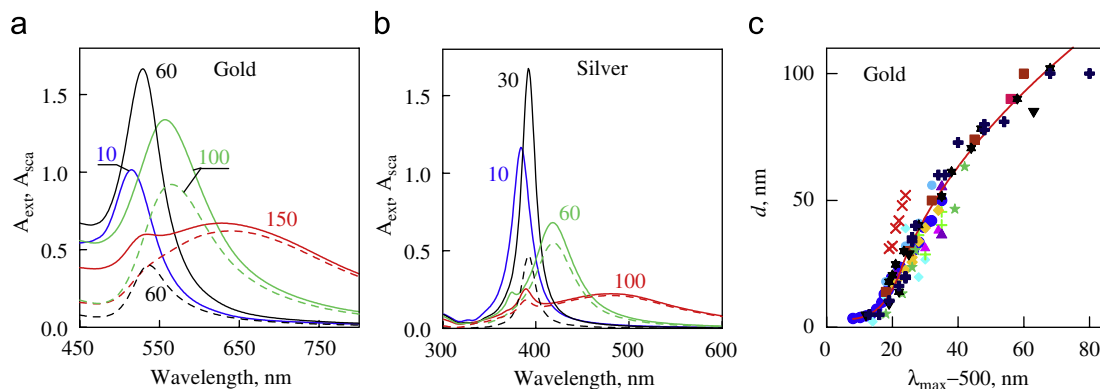
Fig. 6. Extinction (solid lines) and scattering (dashed lines) spectra of gold (a) and silver (b) spheres in water. Numbers near curves correspond to the particle diameter. Panel (c) shows a calibration curve for spectrophotometric determination of the average diameter of CG particles. The symbols present experimental data taken from 14 sources (see Refs. in [141]).
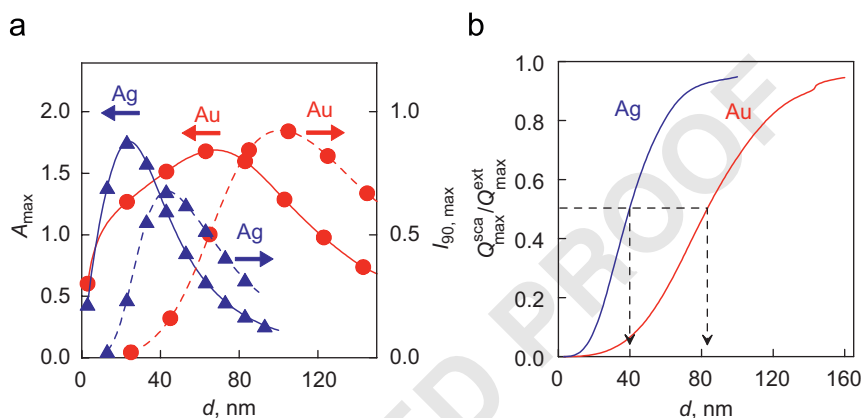

Fig. 7. Dependences of the resonance extinction of suspensions and the intensity of scattering at 90° on the particle diameter at constant weight concentrations of gold (57 μg/ml) and silver (5 μg/ml) (a). Panel (b) shows the ratio of the resonance scattering and extinction efficiencies as a function of particle diameter.

$$d = \begin{cases} 3 + 7.5 \times 10^{-5}X^4, & X < 23 \\ [\sqrt{X-17}-1]/0.06, & X \geq 23 \end{cases}, \quad X = \lambda_{max} - 500.$$

(19)

In practice, this calibration can be used for particles larger than 5–10 nm. For smaller particle, the resonance shifting is negligible, whereas the resonance broadening become quite evident because of size-limiting effects and surface electron scattering [21]. The extinction spectra width also can be used for sizing of fine particles with diameters less than 5 nm [143].

Fig. 7a presents the dependences of the maximal extinction and scattering intensity on the diameter of silver and gold particles. For a constant metal concentration, the maximal extinction is achieved for silver and gold particles of diameters about 25 and 70 nm, respectively. The maximal scattering per unit metal mass can is observed for 40 nm silver and 100 nm gold particles, respectively. Fig. 7b presents the size dependence of the integral albedo at resonance conditions. Small particles mainly absorb light, whereas large particles mainly scatter it. The contributions of scattering and absorption to the

total extinction become equal for 40 nm silver and 80 nm gold particles, respectively.

3.5. Metal nanorods

3.5.1. Extinction and scattering spectra

Fig. 8 shows the extinction and scattering spectra (in terms of the single-particle efficiencies) of randomly oriented gold (a, c) and silver (b, d) nanorods with the equivolume diameter of 20 nm and the aspect ratio from 1 to 6.

Calculations were carried out by the T-matrix method for cylinders with semi-spherical ends. We see that the optical properties of rods depend very strongly on the metal nature. First, as the aspect ratio of gold NR is increased, the resonance extinction increases approximately by a factor of five and the Q factor also increases. For silver, vice versa, the highest Q factor is observed for spheres, whereas the resonance extinction for rods is lower. Second, for the same volume and axial ratio, the extinction and scattering of light by silver rods are considerably more efficient. The resonance scattering
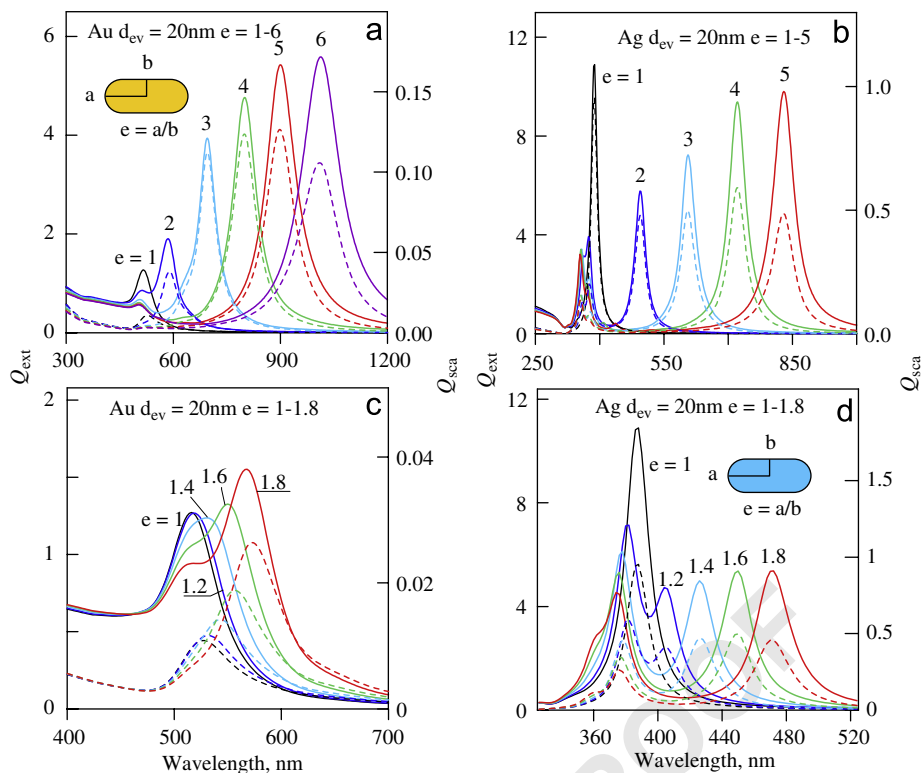
Fig. 8. Extinction (solid curves) and scattering (dashed curves) spectra of randomly oriented gold (a, c) and silver (b, d) s-cylinders with the equivolume diameter 20 nm and the aspect ratio from 1 to 6. Panels (c) and (d) show the transformation of spectra at small deviations of the particle shape from spherical.

efficiencies of silver particles are approximately five times larger than those for gold particles. Third, the relative intensity of the transverse PR of silver particles with the aspect ratio above 2 is noticeably larger than that for gold particles, where this resonance can be simply neglected. Finally, principal differences are revealed for moderate nonspherical particles (Figs. 8c and d). The resonance for gold particles shifts to the red and gradually splits into two bands with dominating absorption in the red region. The scattering band shifts to the red and its intensity increases. For silver rods, the situation is quite different. The short-wavelength resonance shifts to the blue, its intensity decreases and it splits into two distinct bands. In this case, the intensity of the long-wavelength extinction band remains approximately constant, it is comparable with the short wavelength band intensity and shifts to the red with increasing nonsphericity. The integrated scattering and absorption spectra approximately reproduce these features.

The position of the longitudinal long-wavelength resonance can be predicted from the axial ratio of particles and, vice versa, the average aspect ratio can be quite accurately estimated from the resonance position. Fig. 9 presents calibration dependences for measuring the axial ratio of particles from the longitudinal PR position. Along with the T-matrix calculations for s-cylinders of different diameters, we present our and literature experimental data (for details, see Ref. [21]). In the dipolar limit, the plasmon resonance wavelength is completely deter-

mined by the particle shape. However, when the particle diameter is increased, the results of a rigorous solution noticeably differ from the limiting electrostatic curve obtained in the dipole approximation (Fig. 9). This fact was shown for the first time for s-cylinders [144] by the T-matrix method and for right cylinders [145] by the DDA method. Analogous calculations have been extended for larger gold s-cylinders with using T-matrix method [146] and the BEM in a full electromagnetic calculation [147] (see also a close study [148]).

3.5.2. Depolarized light scattering

If colloidal nonspherical particles are preferentially oriented by an external field, the suspension exhibits anisotropic properties such as dichroism, birefringence, and orientation-dependent variations in turbidity and in light scattering. Moreover, even for *randomly* oriented particles, there remain some principal differences between light scattering from nanospheres and that from nanorods. Indeed, when randomly oriented nonspherical particles are illuminated by linearly polarized light, the cross-polarized scattering intensity occurs [118,144] whereas for spheres this quantity equals zero.

The cross-polarized scattered intensity I_{vh} can be characterized by the depolarization ratio $\Delta_{vh} = I_{vh}/I_{vv}$, where the subscripts "$v$" and "$h$" stand for vertical and horizontal polarization with respect to the scattering plane. According to the theory of light scattering by small particles, the maximal value of the depolarization ratio
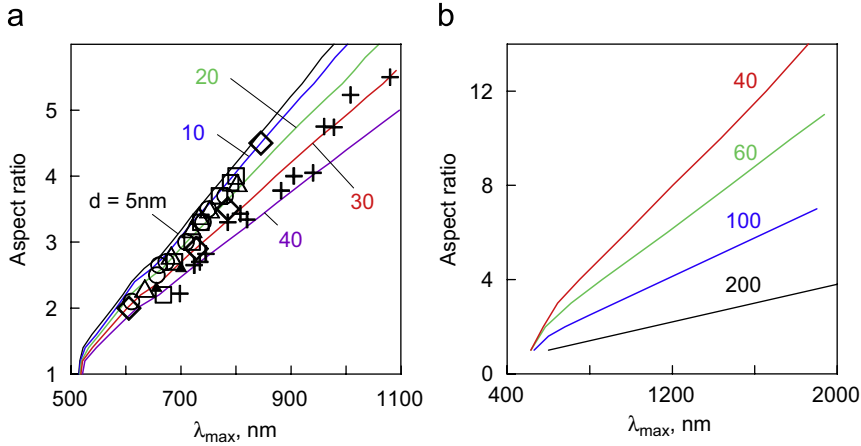
Fig. 9. (b) Calibration plots for determination of the particle aspect ratio through the longitudinal resonance wavelength. Calculations for randomly oriented 5–40 nm gold s-cylinders in water by T-matrix method [144]. The symbols show experimental points (for details, see [87]). (b) Calibration plots for thick 40–200 nm Au s-cylinders calculated by the BEM at perpendicular rod orientation and TM excitation (adapted from Ref. [147]).
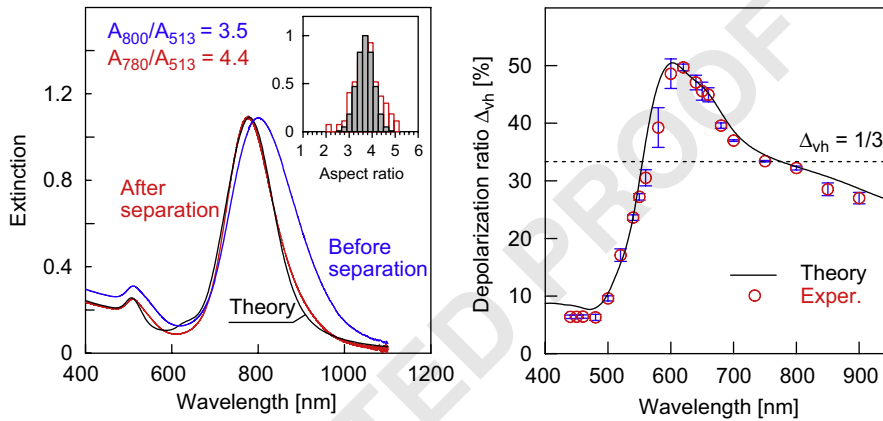

Fig. 10. (a): Extinction spectra of the NR-780 sample before and after separation, together with T-matrix calculations based on best-fitting data ($e_{av} = 3.7$, $\sigma = 0.1$, $W_c = 0.06$). The inset shows a comparison of TEM aspect distribution (light columns) with normal best-fitting distribution (dark columns) for the same sample taken after separation. (b) Experimental and simulated depolarization spectra. The error bars correspond to three independent runs, with analog and photon-counting data included. The dashed line shows the dielectric-needle limit $\frac{1}{3}$.

Δ_{vh} cannot exceed $\frac{1}{3}$ and $\frac{1}{8}$ for dielectric rods and disks with positive values of the real and imaginary parts of dielectric permeability. However, the dielectric limit $\frac{1}{3}$ does not hold for plasmon-resonant nanorods whose theoretical depolarization limit equals $\frac{3}{4}$. [144].

Quite recently, the first measurements of the depolarized light scattering spectra from suspensions of gold nanorods have been reported for 400–900 nm spectral interval [149]. For separated, highly monodisperse and monomorphic samples, we observed depolarized light scattering spectra with unprecedented depolarization ratio of about 50% at wavelengths of 600–650 nm, below the long-wavelength 780 nm extinction peak (Fig. 10). These unusual depolarization ratios are between $\frac{1}{3}$ and $\frac{3}{4}$ theoretical limits established for small dielectric and plasmon-resonant needles, respectively.

To simulate the experimental extinction and depolarization spectra, we introduce a model that included two particle populations: (1) the major nanorod population

and (2) a by-product particle population with the weight fraction $0 \leq W_b \leq 0.2$. The optical parameters were calculated for both populations and then were summed with the corresponding weights W_b and $W_{rods} = 1 - W_b$. The nanorod population was modeled by $N = 10–20$ fractions of rods possessing a constant thickness $d = 2b$, whereas their aspect ratios were supposed to have normal distribution $\sim \exp[-(e/e_{av} - 1)^2/2\sigma^2]$. The average value e_{av} and the normalized dispersion σ were obtained from TEM data and were also considered to be fitting parameters for best agreement between measured and calculated extinction and depolarization spectra. T-matrix calculations with these parameters resulted in excellent agreement between measured and simulated spectra (Fig. 10). Thus, we have developed a fitting procedure based on simultaneous consideration of the extinction and depolarization spectra. This method gives an aspect ratio distribution for the rods in solution from which the average value and the standard deviation can be accu-
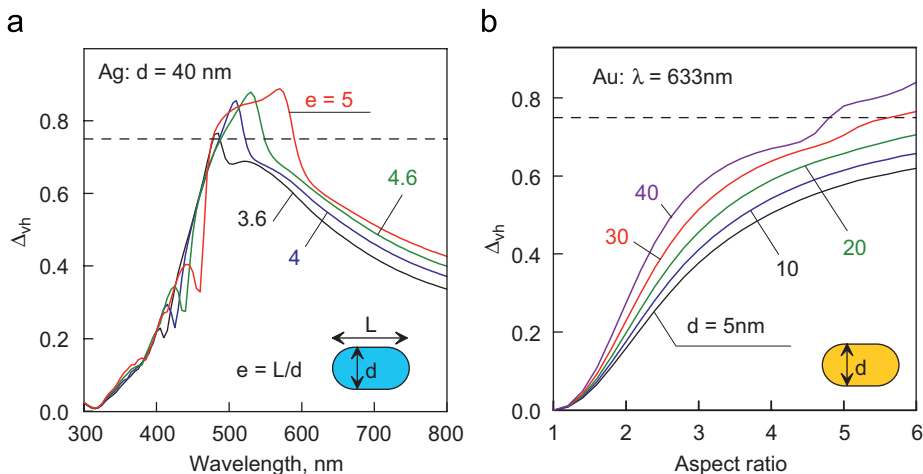
Fig. 11. Spectral dependences of the depolarization ratio for randomly oriented silver s-cylinders of diameter $d = 40$ nm and aspect ratios 3.6–5 (a) and the dependence of the depolarization ratio on the aspect ratio calculated for gold s-cylinders in water at different particle diameters from 5 to 40 nm. (b)
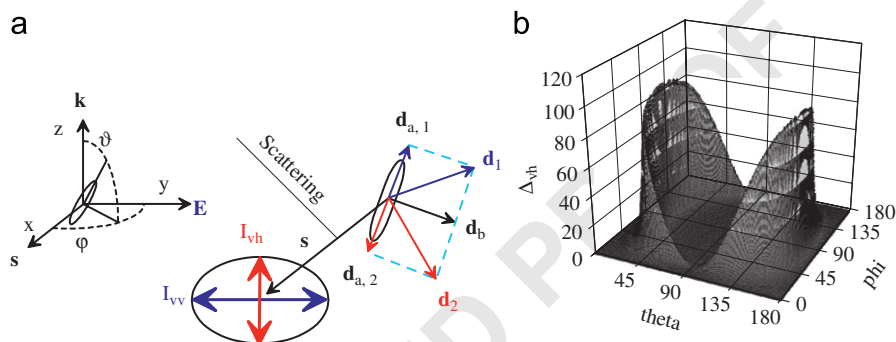

Fig. 12. (a) Scheme to explain the physical origin of enhanced depolarization [150]. The incident light propagates along the z-axis and is scattered along the x-axis, the particle orientation is specified by spherical angles ϑ and φ. (b) 3D plot of the depolarization ratio as a function of angles ϑ and φ. Calculations by the extended precision T-matrix code for gold s-cylinder in water. The rods diameter and length are 20 and 80 nm, respectively, the wavelength 694 nm corresponds to the spectral depolarization ratio maximum.

rately determined in a more convenient and less expensive way than by the traditional TEM analysis.

For larger particles, our T-matrix simulations predict multiple-peak depolarization spectra and unique depolarization ratios exceeding the upper dipolar limit ($\frac{3}{4}$) because of multipole depolarization contributions (Fig. 11).

To elucidate the physical origin of strong depolarization [150], let us consider the scattering geometry depicted in Fig. 12, where the incident x-polarized light travels along the positive z direction and the scattered light is observed in the plane (x, z) in the x-direction. If the particle symmetry axis is directed along the x, y, or z axis, then no depolarization occurs because of evident symmetry constrains. Moreover, no depolarization occurs either for any particle located in the (x, y) or (x, z) plane. Thus, the maximal depolarization contribution is expected from particles located in the (y, z) plane. For usual dielectric rods, the induced dipoles $\mathbf{d}_b$ and $\mathbf{d}_{a,1}$ oscillate in phase. Accordingly, the deviation of the resultant dipole $\mathbf{d}_1$ from the exciting electric field direction is small. Thus, the depolarized scattering should be weak. However, for metal nanorods, the perpendicular ($\mathbf{d}_b$) and longitudinal

($\mathbf{d}_{a,2}$) dipoles can be excited in opposite phases. In this case, the direction of the resultant dipole $\mathbf{d}_2$ can be close to the z-axis direction, thus causing the appearance of significant depolarization.

Fig. 12b shows the orientation dependence of the depolarized light scattering calculated for 20×80 nm gold s-cylinder in water. The scattering geometry is depicted in panel (a). The wavelength of 694 nm corresponds to the maximum of the depolarization spectrum calculated at optimal orientation angles $\vartheta = 20°$ and $\varphi = 96°$. It follows from Fig. 12b that there exists two orientation planes ($\vartheta = 20°$ and $\vartheta = 150°$) where gold nanorods can produce unusual depolarization ratio up to 100% provided that the particle azimuth is close to 90°. Thus, the experimental 50% depolarization maximum is caused by particles located near these optimal orientations.

3.5.3. Multipole plasmon resonances

Compared to numerous data on the dipole properties of nanorods published in the last years, the studies of multipole resonances are quite limited. The first theoretical studies concerned the quadrupole modes excited in

silver and gold spheroids, right circular and s-cylinders, as well as in nanolithographic 2D structures such as silver and gold semispheres and nanoprisms [21]. Recently, the first observations of multipole PRs in silver nanowires on a dielectric substrate [151] and colloidal gold [152] and gold–silver bimetal nanorods [153] were reported.

To elucidate the size and shape dependence of the multipole plasmons, two studies have been performed by using T-matrix formalism [146] and the BEM [147]. Specifically, an extended-precision T-matrix code was developed to simulate the electrodynamic response of gold and silver nanorods whose shape can be modeled by prolate spheroids and cylinders with flat or semispherical ends (s-cylinders). Here, we present a brief summary of the most important results [146]. The multipole extinction, scattering, and absorption contributions are expressed in terms of the corresponding or efficiencies:

$$Q_{ext,sca,abs} = \sum_{l=1}^{N} q_{ext,sca,abs}^{l}. \tag{20}$$

For randomly oriented particles, the multipole partial contributions are given by the equation

$$q_{ext}^{l} = (2/k^2 R_{ev}^2) \text{Spur}_l(T_{\sigma\sigma}), \tag{21}$$

where $\sigma \equiv (l, m, p)$ stands for the T-matrix multiindex and the trace (Spur) is taken over all T-matrix indices except for the multipole order l. For particles at a particular fixed orientation (specified by the angle α between the vector $\mathbf{k}$ and the nanorod axis $\mathbf{a}$), we consider two fundamental cross sections corresponding to the transverse magnetic (TM) and transverse electric (TE) plane wave configurations, where $\mathbf{E} \in (\mathbf{k}, \mathbf{a})$ plane in the TM case and $\mathbf{E} \perp (\mathbf{k}, \mathbf{a})$ plane in the TE case (Fig. 13).

Fig. 13 show the scattering geometry and the extinction, scattering, and absorption spectra of a gold s-cylinder (diameter 40 nm, aspect ratio 6) for the longitudinal, perpendicular (TM polarization), and random orientations with respect to the incident polarized light (a–d). The spectral resonances are numbered according to the designation $Q_{ext}^n \equiv Q_{ext}(\lambda_n)$, $n = 1, 2, \ldots$ from far infra-red to visible, whereas the symbol "0" designates the shortest wavelength resonance located near the TE mode. Three important remarks can be made on the basis of the plots in Fig. 13a–d. First, the maximal red-shifted resonance for random orientations is due to TM dipole ($n = 1$) excitation of particles, whereas the short-wavelength "zero" resonance is excited by TE polarization of the incident light. Second, both scattering and absorption resonances have the same multipole order, are located at the same wavelengths, and give comparable contributions to the extinction for the size and aspect ratio under consideration. Finally, for basic longitudinal or perpendicular orientations, some multipoles are forbidden because of the symmetry constrains.

Consider now the case of strongly elongated particles with an aspect ratio $e = 10$ (panels e.g.). In this case, the random orientation spectra exhibit a rich multipole structure that includes multipole resonances up to $n = 5$. As in the previous case, at a minimal thickness $d = 20$ nm, the scattering contribution is negligible, and all reso-

nances are caused by the absorption multipoles. Note also that the short-wavelength resonance has negligible amplitude. With an increase in the particle thickness from 20 to 40 and further to 80 nm, all resonances move to the red region, and new scattering and absorption high-order multipoles appear. Again, the scattering contributions dominate for large particles, whereas at moderate thicknesses the scattering contribution is comparable to or less than the absorption contribution, except for the long-wavelength dipole resonance of number 1.

Fig. 13i shows the extinction spectra $Q^{ext}(\lambda)$ of randomly oriented gold spheroids with a minor axis $d = 80$ nm and an aspect ratio $e = 10$ (data for s-cylinders see in Ref. [146]). Besides the usual long-wavelength dipole resonance (not shown), five additional multipole resonances can be identified (the 6th resonance looks like a weak shoulder, but it is clearly seen on the multipole contribution curve, designated q_6). A close inspection of spectra leads to the following conclusions: (1) The parity of multipole contributions coincides with the parity of the total resonance. (2) For a given spectral resonance number n, the number of partial multipole contributions l is equal to or greater than n. This means that the multipole q_1 does not contribute to the resonances $Q^{2n+1}(n \geq 1)$, the multipole q_2 does not contribute to the resonances $Q^{2n}(n \geq 1)$, and so on. Note that the second statement of the multipole contribution rule is, in general, shape dependent [146]. To elucidate the scaling properties of the multipole resonances, we carried out extensive calculations for various nanorod diameters and aspect ratios. The general course of λ_n vs the e plots show an almost linear shift of the multipole resonances with an increase in aspect ratio

$$\lambda_n = f(e/n) \simeq A_0 + A\frac{e}{n}. \tag{22}$$

Fig. 13j illustrates the scaling law (22) for randomly oriented gold spheroids ($d = 80$ nm, $e = 2 - 20$) in water. It is evident that for resonance numbers $n = 1-8$, all data collapse into single linear functions. Physically, this scaling can be explained in terms of the standing plasmon wave concept and the plasmon wave dispersion law, as introduced for metal nanoantennas [154]. A very simple estimation of the resonance position is given by the equation

$$n\frac{\pi}{L} = \frac{2\pi}{\lambda_n^{eff}} = q^{eff}(\omega_n), \tag{23}$$

where $q^{eff}(\omega_n)$ is an effective wave number corresponding to the resonance frequency ω_n. At a constant particle thickness, d, Eq. (32.20) predicts a linear scaling (23) $\lambda_n^{eff} \sim L/n \sim de/n \sim e/n$, in full accord with our finding given by Eq. (22).

3.6. Coupled plasmons

Along with the optics of individual PR particles, the collective behavior of the interacting PR particles is of great interest for nanobiotechnology [140,155]. The analysis of its features includes the study of various structures, beginning from 1D chains with unusual optical

Fig. 13. Two basic TE and TM polarizations of incident light. The orientation of a particle is specified by an angle α between the wave vector **k** and the particle symmetry axis **a**. Panels (a–d) show the extinction, scattering, and absorption spectra of gold s-cylinders for longitudinal, perpendicular TE, perpendicular TM, and random orientations of gold nanorod with respect to the incident polarized light. Panels (e–h) show variation of spectra with an increase in the rod diameter at a constant aspect ratio $e = 10$. The numbers near the curves designate multipole orders according to the T-matrix assignment. (i): Extinction spectra $Q^{ext}(\lambda)$ of randomly oriented gold spheroids with a thickness $d = 80$ nm and an aspect ratio $e = 10$. The curves $q_1 - q_6$ show the spectra of multipole contributions. The upper row of numbers $n = 2–6$ designates the total resonances $Q^n = Q_{ext}(\lambda_n)$. The resonance Q^1 is located in the far infrared region and is not shown. (j): Linear scaling of the multipole resonance wavelengths λ_n vs the normalized aspect ratio e/n. The regression scaling equation is shown in the plot.

properties [156]. Another example is the optics of 2D arrays [140,155,157,158], in particular, clusters of spherical particles on a substrate and 2D planar ensembles formed by usual gold or polymer-coated spheres [155]. The unusual properties of monolayers of silver NPs in a polymer film [159,160] and gold or silver NPs and NSs in water or on a glass substrate [161] have been recently discovered. A review of 3D sphere-cluster optics can be found in Refs. [5,139,155].

Apart form direct numerical simulations (e.g., MMP simulation of disk pairs on a substrate [162] and FEM simulations of silver sphere-clusters [163]) or an approx-

imate electrostatic considerations [164], a new concept called "the plasmon hybridization model" [129,130] has been developed to elucidate basic physics behind plasmon coupling between optically interacting particles.

A more complex assembly of high aspect ratio gold NRs on a substrate has been studied in Ref. [165]. The long axes of NRs were oriented perpendicularly to the substrate. The optical response of such an assembly was governed by a collective plasmonic mode resulting from the strong electromagnetic coupling between the dipolar longitudinal plasmons supported by individual NRs. The spectral position of this coupled plasmon resonance and the associated electromagnetic field distribution in the nanorod array were shown to be strongly dependent on the inter-rod coupling strength.

The unique properties of strongly coupled metal particles are expected to find interesting applications in such fields as the manipulation of light in nanoscale waveguide devices, sensing and nonlinearity enhancement applications, and the subwavelength imaging. As an example, we can refer to recent work by Reinhard et al. [166]. These authors extended the conventional gold particle tracking with the capability to probe distances below the diffraction limit using the distance dependent near-field interactions between individual particles. This

technology was used for precise monitoring the interaction between individual gold nanoparticles on the plasma membrane of living HeLa cells.

As the coupled plasmonics is extremely fast growing field, the number of related works exceeds the scope of this review. Therefore, we have to restrict our consideration by only several instructive examples, including gold and silver interacting bispheres, gold linear chains, and a monolayer of interacting nanoparticles on a substrate.

3.6.1. Metal bispheres

Fig. 14a,b shows the absorption spectra calculated by multipole method [167] for two gold particle diameters $d = 15, 30$ (data for 60 nm see in Ref. [139]) separated by a variable distance s. When the interparticle separation satisfies the condition $s/d \geq 0.5$, the absorption efficiencies approach the single-particle quantities and the dipole and multipole calculations give identical results [139]. However, the situation changes dramatically when the relative separation s/d is about several percent. The coupled spectra demonstrate quite evident splitting into two components with pronounced red-shifting of the long-wavelength resonance when the spheres approach each other.
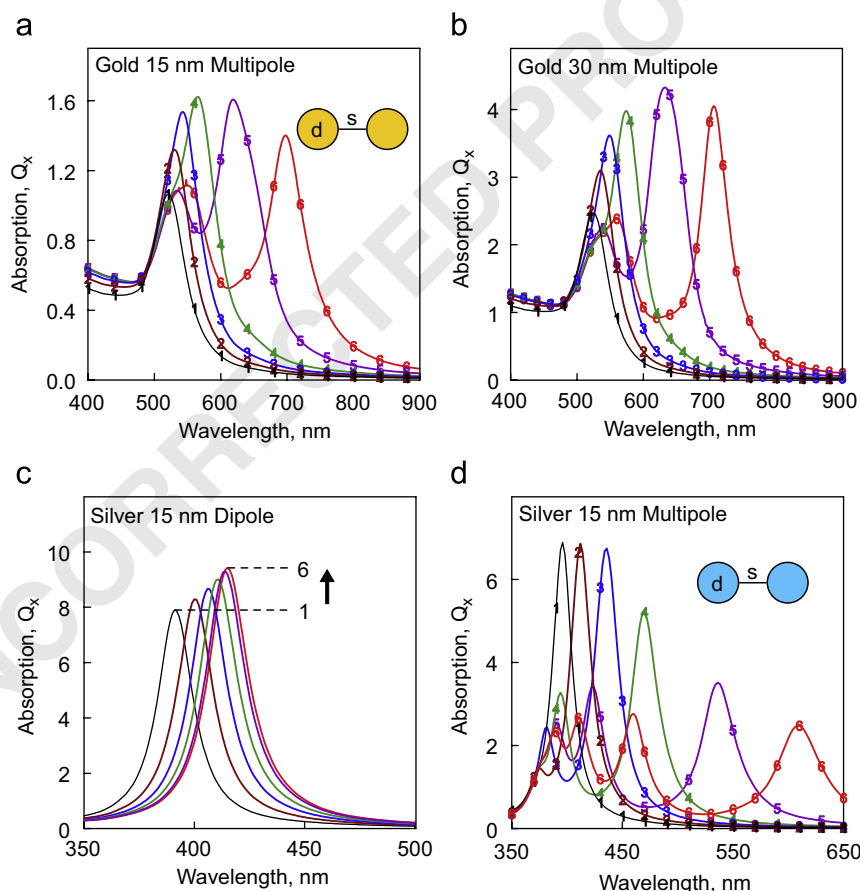

Fig. 14. Absorption spectra at an incident light polarization parallel to the bisphere axis ($x \equiv \parallel$). Calculations by the exact GMM multipole code (a,b,d) and dipole approximation (c) for gold (a,b) and silver (c,d) particles with diameters $d = 15$ (a,c,d) and 30 nm (b) and the relative interparticle separations $s/d = 0.5$ (1), 0.2 (2), 0.1(3), 0.05 (4), 0.02 (5), 0.01 (6).

In the case of silver bispheres (Fig. 14c,d), the resonance light scattering of 60 nm clusters exceeds the resonance absorption so that any comparison between the dipole and the multipole approaches becomes incorrect unless both scattering and absorption are taken into account for the total extinction. That is why we show only the calculated data for silver nanospheres with $d = 15$ nm. At moderate separations ($s/d > 0.05$), the independent-particle spectrum splits into two modes; therefore, the data of Fig. 14c,d are in great part analogous to those for independent particles. However, at smaller separations $s/d < 0.05$, we observe the appearance of four plasmon resonances related to the quadrupole and the next high-order multipole excitations. The exact multipole approach predicts the well-known enormous theoretical [155] and experimental [168] red-shifting of spectra and their splitting [169] into two modes, whereas the dipole spectra show only a minor red shift (Fig. 15c). 14c

The dependence of the extinction spectra on the total multipole order N_M was studied in Refs. [139,155]. Note that N_M means the maximal order of vector spherical harmonics (VSH) retained in the coupled equations rather than the number of multipoles involved in the final calculations of optical characteristics. According to computer experiments (Fig. 15), one has to include extra-high single-particle multipole orders (up to 30–40) into coupled equations to calculate correctly the extinction spectra of 15 nm gold spheres separated by a 0.5–1% relative distance s/d. The need to retain high multipoles for small spheres, which are themselves well within the dipole approximation, seems to be somewhat counter-intuitive. It should again be emphasized that the final calculations involve rather small number of multipoles (as a rule, less than 6). However, to find these small-order contributions correctly, one needs to include much more multipoles into coupled equations. The physical origin of this unusual electrodynamic coupling was first established by Mackowski [170] for small soot bispheres. He showed that the electric-field intensity can be highly inhomogeneous in the vicinity of contact point between the spheres even if the external filed is homogeneous on

the scale of bisphere size. Evidently, the same physics holds in our case, as the imaginary part of the dielectric permittivity is the main parameter that determines the spatial electric-field distribution near the contact bisphere point.

3.6.2. Linear chains and square lattices

To gain insight into the mechanisms determining the effect of particle aggregation on the absorption efficiency, it is useful to considered simple 1D linear chains and 2D lattice square arrays from metal (here, gold) spheres of a diameter d and separated by the interparticle distance s. In both cases, the incident TE and TM electromagnetic waves are directed perpendicularly to the cluster axis or the cluster plane. For a linear chain, TM polarization means that the electric vector of an EM wave is directed along the chain axis, whereas for 2D square arrays both polarizations are equivalent. The absorption spectra of 1D and 2D clusters can be characterized in terms of the *normalized cross section* defined as

$$F(\lambda) = C_{abs}(\lambda)/NC_{abs1}(\lambda_{max}), \tag{24}$$

where λ is the wavelength in vacuum, N is the number of cluster particles, and $C_{abs1}(\lambda_{max})$ is the absorption cross section of a single sphere at the plasmon resonance wavelength ($\lambda_{max} = 520$ nm for small gold spheres). In the case of a specific irradiation wavelength λ_0 (e.g., $\lambda_0 = 800$ nm), we also used the *amplification factor* at a particular wavelength, defined as

$$F_a(\lambda_0) = C_{abs}(\lambda_0)/NC_{abs1}(\lambda_0) \tag{25}$$

Fig. 16 shows normalized spectra of linear gold sphere chains in terms of the normalized cross section, as defined by Eq. (24). These spectra are for two particle numbers 4 and 32 (other examples can be found in Ref. [140]) and for different relative interparticle distances s/d, beginning with the non-interacting particles to closely packed chains with $s/d = 0.025$.

In the general case, there are two characteristic absorption maxima of linear chains. The short wavelength maximum corresponds to the plasmon resonance of
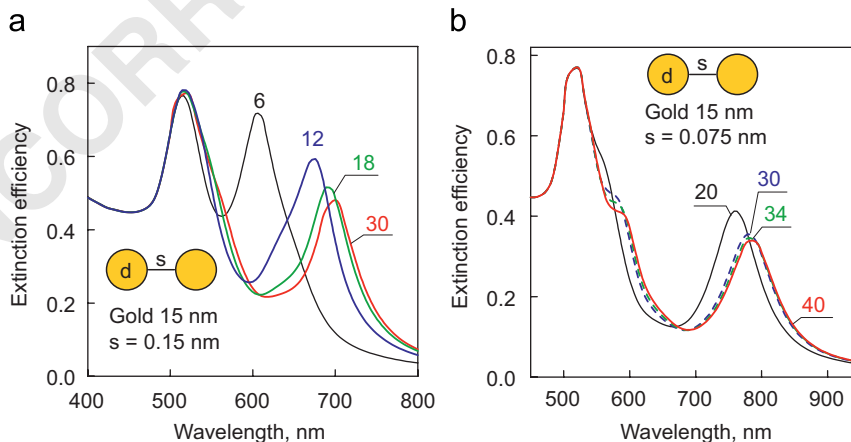
Fig. 15. Extinction spectra of 15 nm randomly oriented gold bispheres in water calculated by the exact T-matrix method for separation distances between spheres 0.15 nm (a) and 0.075 nm (b). The numbers near the curves designate the multipole orders included in the single-particle field expansions of coupled equations.
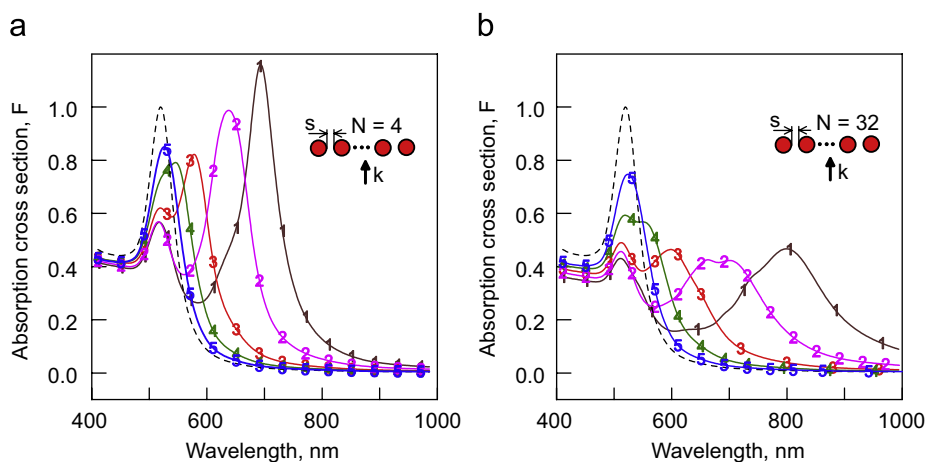
Fig. 16. Normalized absorption spectra of linear chains in water at perpendicular excitation by an unpolarized incident wave. The cluster particle numbers are 4 (a) and 32 (b); the particle diameter is 40 nm; and the normalized interparticle distances s/d are 0.025 (1), 0.05 (2), 0.125 (3), 0.25 (4), and 0.5 (5). The dashed curve corresponds to the noninteracting spheres.

monomers excited by the TE mode of incident light (the electric vector oscillates perpendicularly to the chain). The other, long-wavelength resonance appears at the electric excitation of the chain along its axis and is due to the strong electrodynamic coupling of chain spheres. In the case of unpolarized incident light, both modes are seen in the spectra. Analogous properties have been found for silver nanoshell chains [171].

A comparison with Fig. 8 reveals an evident analogy between the longitudinal plasmon resonance of metal nanorods and the longitudinal resonance of linear chains. One can say that a linear chain of coupling spheres absorbs and scatters light like an "equivalent" solid metal rod does. However, unlike solid rods, the linear chains exhibit the extinction spectra show of richer structure. For instance, the longitudinal peak position depends not only on the aspect ratio but also on the separation between neighboring particles. Besides, the single-sphere resonance is clearly seen in Fig. 16 whereas the corresponding rod resonance looks as a spectral shoulder. It is evident from computer simulations that the maximum possible increase in absorption per particle is achieved at long-itudinal excitation, and the desired tissue-optic tuning to 800 nm may be obtained for chains consisting of as many as 10 particles. In this case, the absorption amplification is about 50–120%.

We also observed some saturation in the absorption amplification for long chains. This effect is more evident from Fig. 17 where the extinction and scattering spectra are shown for linear chains of two-layered nanospheres with a gold core and a dielectric shell [155]. Such particles serve as a model of NP conjugates [172]. The number of conjugates in Fig. 17 is the variable parameter of curves. It is worth noting a principal difference between the spectra of densely packed metal spheres (shell thickness $t = 1$ nm, strong binary coupling, Fig. 17c,d) and rare metallic chains ($t = 5$ nm, weak binary coupling, Fig. 17a,b). The extinction spectra do not change essentially for the case $t = 5$ nm (Fig. 17a), while the plasmon resonance peak in the scattering spectra increases significantly due to construc-

tive far-field interference. However, the peak position does not shift significantly. For a thin dielectric shell of about 1 nm, the transformation of extinction and scattering spectra are due to both the electrodynamic coupling and the far-field interference. Again we observe a rapid saturation of spectra with an increase in the chain particle number. In other words, beginning from a particular number of interacting spheres (say, about of 10), the extinction or scattering spectra of a long linear chain become insensitive to the total number of constitutive spheres. This can be explained by an effective electro-dynamic interaction between monomers which belong to a finite conjugate group [155].

The dimensionless amplification factor (Eq. (25)) is defined as the ratio of cluster absorption to the sum of single-particle absorptions. Fig. 18a shows that this parameter is determined mainly by the relative inter-particle distance in a universal manner and that the calculated curves $F_a(s/d)$ collapse into a universal depen-dence if the number of particles is > 4. Similar results have been obtained for lattice 2D arrays (Fig. 18b). It follows from these graphs that a significant increase in the amplification factor can be achieved by decreasing the relative interparticle distance down to $s/d < 0.1$. It should be stressed that the drop in amplification of well separated chains is due primarily to the resonance moving away from 800 nm.

3.6.3. Universal plasmon ruler

With use of gold NP-DNA conjugates, Reinhard et al. [173] reported a detailed calibration of the plasmon peak position versus bisphere separation for 42 and 87 nm-diameter gold particles. The experimental resonance wavelengths as a function of interparticle separation were found to be in agreement with the T-matrix calculations by Wei et al. [174] and with the so-called "universal plasmon ruler" (UPR) equation (see, e.g., [175] and references therein):

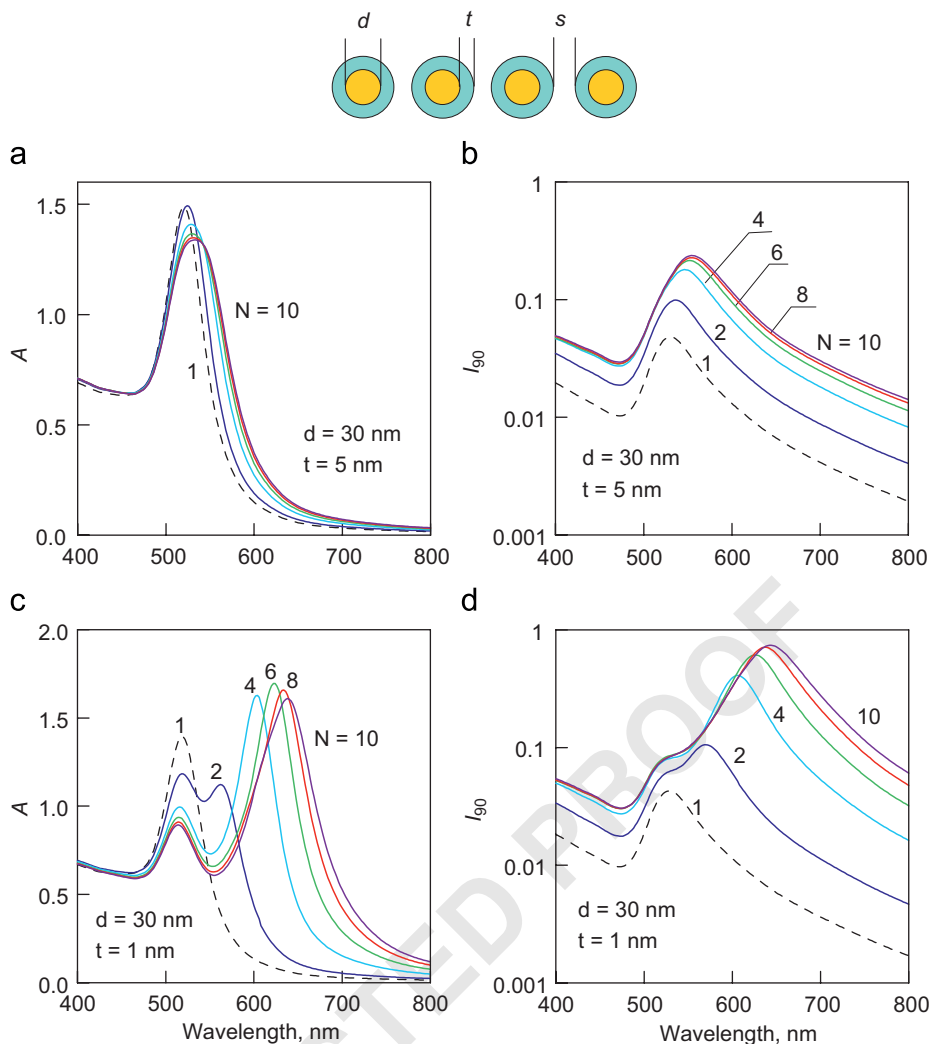$$\Delta\lambda = A\exp[-B(s/L)] + C. \tag{26}$$

Fig. 17. Extinction and scattering spectra of randomly oriented linear chains of two-layered conjugates with different conjugate number $N = 1-10$. Calculations for the core diameter $d = 30$ nm, shell thickness $t = 5$ (a, b) and 1 nm (c, d), and separation distance $s = 0$.

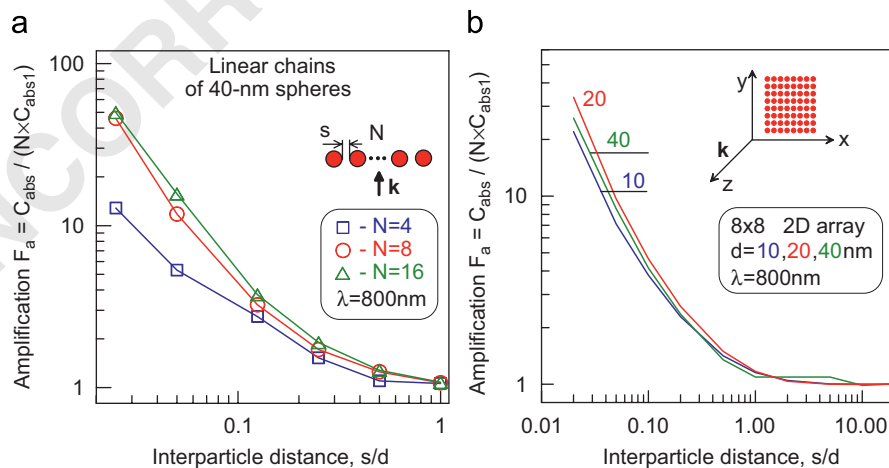
Fig. 18. The dependence of absorption amplification at 800 nm on the normalized interparticle distance of linear 4-, 8-, and 16-particle chains of 40 nm spheres (a) and 8×8 2D arrays of 10, 20, and 40 nm spheres (b) [140].
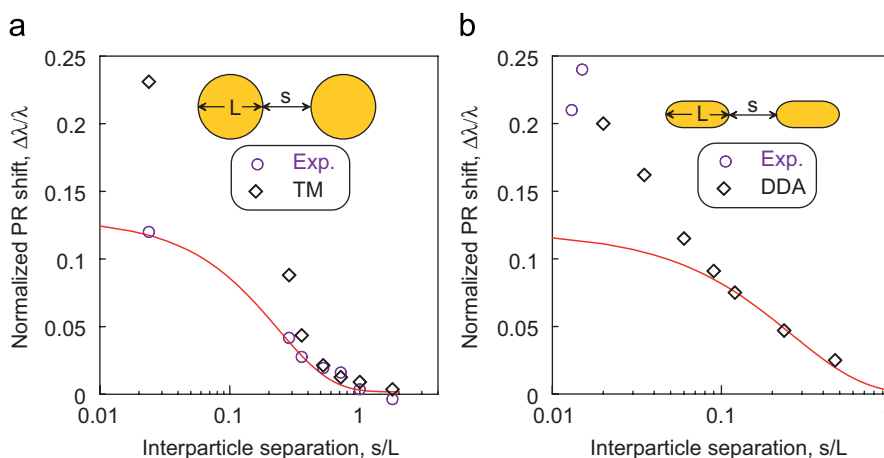
Fig. 19. Normalized PR shift of two 48 nm gold spheres (a) and gold s-cylinders (b) as a function of interparticle distance scaled for sphere diameter or nanorod length. Experimental points are adapted from Ref. [173] (a) and [176] (b). Simulations were carried out by T-matrix [139] (a) and DDA [176] (b) methods. Solid curves show the UPR fits. Medium refractive index is 1.6 (a) and 1.56 (b).

where $\Delta\lambda$ is the PR shift caused by the particle optical coupling, L is a characteristic size (e.g., L is a sphere diameter or NR length), and A, B and C are the fitting constants. In essence, the UPR means a universal dependence of the couple resonance shift determined only by the separation distance normalized to the characteristic particle size. In particular, the UPR has been confirmed in simulations [162,175].

Fig. 19a shows experimental points and UPR curve (adapted from Ref. [173]) together with our T-matrix calculations (adapted from Ref. [139]). In accord with Ref. [173], we found good agreement between the experimental data and the T-matrix curve within the separation range $0.2 \leq s/d \leq 2$. However, the single-exponential fit (26) does not match the general character of T-matrix curves at small separations $s/d \leq 0.2$.

Quite recently, Mulvaney et al. [176] reported experimental scattering spectra of gold nanorod dimers arranged in different orientations and separations. The spectra exhibited both red- and blue-shifted surface plasmon resonances, consistent with both the DDA simulations and the plasmon hybridization model. Fig. 19b shows experimental points and DDA simulations for the normalized PR shift caused by interaction of two gold NRs (adapted from Ref. [176]). The solid curve shows UPR fit over the first 4 DDA points at maximal separations. Clearly, both pictures (a) and (b) demonstrate very close behavior. These plots show that the approximation of the coupling distance dependence according to the dipole–dipole approximation or as an exponential may be not valid for normalized separations less than 0.1. Perhaps, the above deviations from UPR are related to the strong multipole interactions excited at extra small separation distances. For a more detailed theoretical treatment, see Ref. [177].

3.6.4. Monolayers of metal nanoparticles and nanoshells

Recently, Chumanov et al. [159,160] found an unusual behavior of the extinction spectra for a monolayer of interacting silver nanoparticles embedded in a polymer film. Specifically, they showed an intense sharpening of the quadrupole extinction peak resulting from selective suppression of the coupled dipole mode as the interparticle distance becomes smaller. This phenomenon was explained qualitatively by using simple symmetry considerations.

A comprehensive theoretical analysis of a monolayer consisting of metal or metallodielectric nanoparticles with the dipole and quadrupole single-particle resonances has been done in Ref. [161]. The theoretical models included spherical gold and silver particles and also gold and silver nanoshells on silica and polystyrene cores forming 2D random clusters or square-lattice arrays on a dielectric substrate (glass in water). The parameters of individual particles were chosen so that a quadrupole plasmon resonance could be observed along with the dipole scattering band. By using an exact multipole cluster-on-a-substrate solution, it has been shown that particle-substrate coupling can be neglected in calculation of the monolayer extinction spectra, at least for the glass-in-water configuration. When the surface particle density in the monolayer was increased, the dipole resonance became suppressed and the spectrum for the cooperative system was determined only by the quadrupole plasmon. The dependence of this effect on the single-particle parameters and on the cluster structure was examined in detail. In particular, the selective suppression of the long-wavelength extinction band was shown to arise from the cooperative suppression of the dipole scattering mode, whereas the short-wavelength absorption spectrum for the monolayer was shown to be little different from the single-particle spectrum.

Here, we provide only several illustrative examples. As a simple monolayer model, we used a square lattice with a period $p = d_e(1 + s)$, where d_e is the external diameter of particles and s is the relative interparticle distance. Another monolayer model was obtained by randomly filling a square of side L/d_e with a given number of
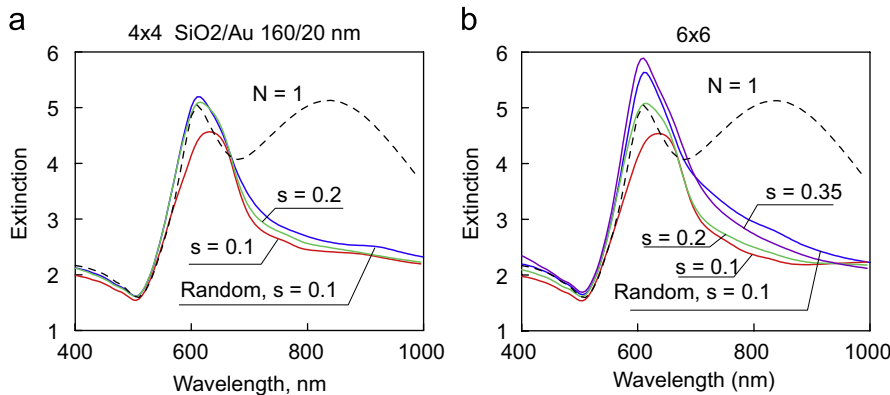
Fig. 20. Comparison of the extinction spectra for lattice (4×4, 6×6) and random clusters made up of SiO_2/Au ($160/20\,nm$) nanoshells with particle numbers of 16 (a) and 36 (b). Also shown are the spectra for isolated particles ($N = 1$). The interparticle-distance parameter is 0.1, 0.2, and 0.35 for the lattice clusters and equals 0.1 for the random clusters. The average particle density for the random clusters is 0.415 (a) and 0.36 (b) for 16 and 36 particles, respectively.

particles N. Then, the relative coordinates of the particles X_i were transformed as $x_i = X_i d_e(1 + s)$ where the parameter s controls the minimal interparticle distance. The structure of the resultant monolayer is characterized by the particle number N and the average surface particle density $\rho = NS_{geom}/[L^2(1 + s)^2]$.

The interparticle distance is a crucial parameter determining the electrodynamic particle coupling and the cooperative spectral properties of an ensemble. Therefore, we first investigated the influence of the interparticle-distance parameter s on the suppression of the dipole mode. Fig. 20 shows a comparison of the extinction spectra of lattice and random clusters. All particle and cluster parameters are indicated in the figure caption. It can be seen that in both cases, the spectra for the lattice clusters with an s parameter of 0.2 are much the same as the spectra for the random clusters. Closer agreement between the spectra for the 36-particle clusters can be obtained if the s parameter is 0.35 in the lattice case. Beginning with parameter s values about 0.2, there was effective suppression of the dipole mode, so that the resonance was determined by only the quadrupole mode. A twofold decrease in the s parameter (to as low as 0.1) brought about little change in the system's spectrum. These conclusions are general and depend little on the properties of particles themselves.

To gain an insight into the physical mechanisms responsible for suppression of the coupled dipole mode, one also has to investigate the influence of particle interactions on the cooperative absorption and scattering of light. This question has been studied for several models, including silver and gold spheres as well as silver and gold nanoshells on dielectric cores (polystyrene and silica). In the case of silver spheres, it has been found that the suppression in a monolayer of the dipole extinction band is determined entirely by the decrease in *dipole resonance scattering* that occurs when strongly scattering particles with a dipole and a quadrupole resonance move closer together. The electrodynamic interparticle interaction almost does not change the absorption spectrum, including its fine structure in the short-wavelength region.

Fig. 21 shows the dependence of the extinction, scattering, and absorption spectra for random clusters of 36 20 nm silver nanoshells on 110 nm polystyrene (PS) spheres. The calculated results were averaged over five independent cluster generations. It can be seen that the transformation of the extinction, scattering, and absorption spectra occurring with increasing particle density in the monolayer is similar to that for silver sphere monolayer [161]. Namely, the clear-cut quadrupole and octupole absorption peaks in the short-wavelength portion of the spectrum almost do not depend on the average particle density in the monolayer. As in the case of solid silver spheres, the disappearance of the dipole extinction band is associated with the suppression of the dominant dipole scattering band.

For experimental studies [161], the silica/gold nanoshell monolayers were fabricated by the deposition of nanoshells on a glass substrate functionalized by silane-thiol cross-linkers. The measured single-particle and monolayer extinction spectra were in reasonable agreement with simulations based on the nanoshell geometrical parameters (scanning electron microscopy data). Finally, the sensitivity of the coupled quadrupole resonance to the dielectric environment was evaluated to find a universal linear relation between the relative shift in the coupled-quadrupole-resonance wavelength and the relative increment in the environment refractive index.

We conclude this section by Fig. 22, which shows an SEM image of fabricated monolayer, the single-particle extinction spectra, and the coupled spectra of the monolayer. Calculations with fitting size parameters reproduce the spectral positions of both quadrupole and dipole bands. The quadrupole extinction peak for a particle suspension is located near 760 nm, and the dipole scattering band lies in the near IR region (about 1100 nm). The theoretical single-particle spectrum reveals an octupole resonance near 650 nm, which is not seen, however, in the experimental plots because of the polydispersity and surface roughness effects. A separate calculation of extinction, absorption, and scattering spectra allow us to attribute the octupole peak to the dominant absorption
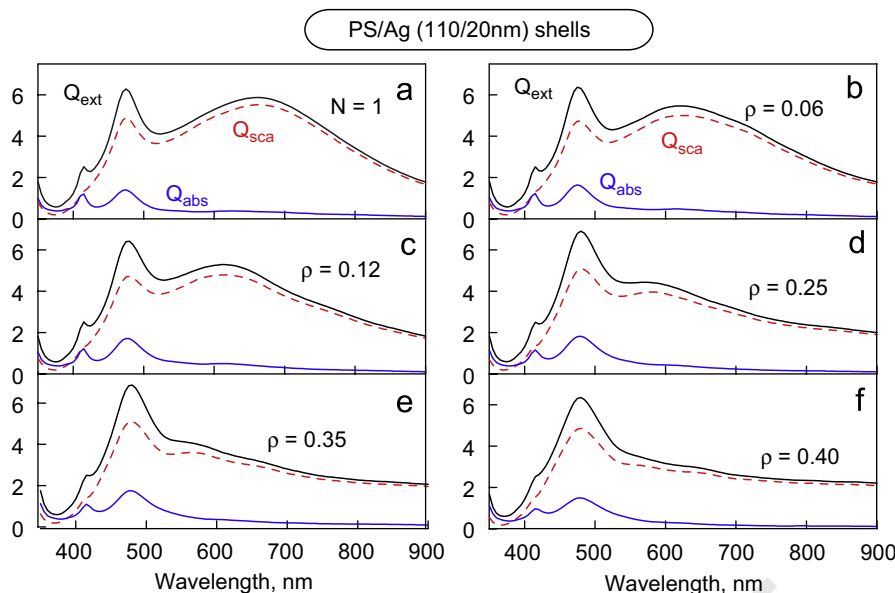
Fig. 21. Extinction, scattering, and absorption spectra for random clusters made up of 36 PS/Ag-type silver nanoshells (core diameter, 110 nm; shell thickness, 20 nm). The minimal-distance parameter *s* is 0.05, and the average particle density is 0 (a, a single-particle), 0.06 (b), 0.12 (c), 0.25 (d), 0.35 (e), and 0.4 (f). The calculated results were averaged over five statistical realizations.
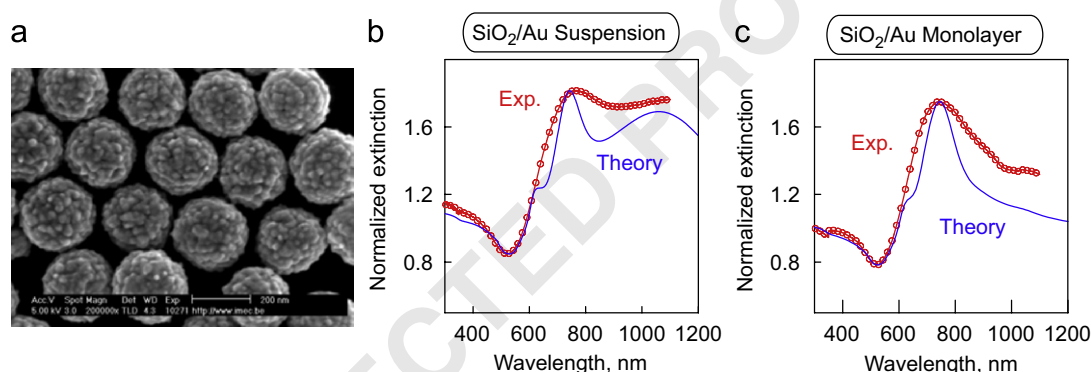

Fig. 22. SEM image of a monolayer portion showing self-assembled silica/gold nanoshells on a silane-functionalized quartz substrate. The average nanoparticle diameter is 245 ± 12 nm, and the average silica core diameter is 200 ± 10 nm (a). Normalized experimental and theoretical extinction spectra for a suspension of nanoshells (b) and for a monolayer on a silane-functionalized quartz substrate in water (c). Details of theoretical fitting can be found elsewhere [161].

resonance, the quadrupole peak to both the scattering and the absorption contribution, and the dipole peak to the dominant scattering resonance. The particle interaction in the experimental monolayer brought about a noticeable decrease in the extinction shoulder (800–1100 nm) because of suppression of the scattering resonance. To simulate the monolayer spectrum, we used the fitting average core diameter and gold shell thickness (230 and 15 nm) and five independent calculations for a random array ($N = 36$) with the average surface particle density $\rho = 0.25$ (the *s* parameter equals 0.05). In general, the model calculations agree well with the measurement. In any case, the suppression of dipole peak is clearly seen in both the experimental and simulated spectra.

4. Biomedical applications

4.1. Functionalization of metal nanoparticles

In nanobiotechnology metal nanoparticles are used in combination with recognizing biomacromolecules attached to their surface by means of physical adsorption or coupling through the Au–S dative bond (for example, single-stranded oligonucleotides [178], antibodies [179], peptides [180], carbohydrates [181], etc.). Such nanostructures are called bioconjugates [1,39,182], while the attachment of biomacromolecules to the NP surface is often called "functionalization" [21,39]. Thus, a probe conjugate molecule is used for unique coupling with a target, while a metal core serves as an optical label.

Metal hydrosols are typical lyophobic colloids [39,40] which are thermodynamically unstable and require special stabilization of particles. For instance, citrate CG particles are stabilized due to negative charge, while the stability of the seed-mediated gold NRs is ensured by CTAB protection. Over last decade, a lot of functionalization protocols have been developed to include various nanoparticles and biomolecules [2,39,180]. The most popular technology is based on using the thiolated intermediate linkers such as $HS(CH_2)nR(R=COOH$, OH or SO_3H; $n = 11-22$) [183], or directly the thiolated derivatives of molecular probes such as oligonucleotides, proteins, immunoglobulins, avidin, and even dual functionalization by thiol-oligonucleotides and antibodies [184]. Besides alkanethiols, other ligands containing phosphino, amino, or carboxy groups can also be used as linkers [2]. Quite recently, a new class of so-called "Mix-matrices" has been proposed to facilitate bioconjugation process [185]. In contrast to usual CG or NS particles, the functionalization of gold NRs encounters significant difficulties because of presence of CTAB surfactant molecules serving as stabilizers (see, e.g., a relevant discussion and comprehensive citations in Ref. [41]). Nevertheless, even for such a complicated task, several publications have demonstrated successful protocols for gold nanorods [186–189]. Wei et al. [63] also provided useful discussion of five functionalization schemes as applied to gold NRs.

An interesting approach to the enzymatic-driven assembly has been reported recently by Alivisatos group [190]. It was shown that DNA ligases, which seal single-stranded nicks in double-stranded DNA (dsDNA), also can operate on thiolated DNA-CG conjugates. Specifically, the enzymatic ligation of single CG-DNA conjugates created NP dimer and trimer structures in which the nanoparticles were linked by single-stranded DNA, rather than by double-stranded DNA. This capability was utilized to create a new class of multiparticle building blocks for nanoscale self-assembly.

At present, most biomedical applications are based on gold-particle conjugates. As for silver particles, we can recommend recent paper [191] where the problem is discussed in general aspects. In addition, in a recent work Huang et al. [192] successfully designed and synthesized silver nanoparticle biosensors (AgMMUA–IgG) by functionalizing 11.6 nm Ag nanoparticles with a mixed monolayer of 11-mercaptoundecanoic acid (MUA) and 6-mercapto-1-hexanol (1:3 mole ratio). Further, these intermediate particles were additionally functionalized by covalently conjugating IgG of with MUA on the nanoparticle surface via a peptide bond using 1-Ethyl-3-(3-dimethylaminopropyl)-carbodiimide hydrochloride EDC and *N*-hydroxysulfosuccinimide as mediators. Such an example clearly demonstrates that the gold and silver particles can be functionalized with biospecific molecules through common or analogous protocols.

4.2. Homogenous and bio-barcode assays

There are two variations of the homogeneous assays based on gold-nanoparticle aggregation: (1) aggregation of "bare" particles or particles covered with synthetic polymers that nonspecifically interact with biomacromolecules and (2) biospecific aggregation of conjugates that is initiated by the binding of target molecules in solution or by the binding of target molecules adsorbed on another conjugate. The ability of gold particles interacting with proteins to aggregate with a solution color change served as the basis for development of a method for the colorimetric determination of proteins [193,194]. As a rule, one uses UV–VIS spectrophotometry of a gold sol (partially stabilized with polymers like Tween-20 or PEG) that can nonspecifically interact with biomacromolecules under acidic condition what is accompanied by change in the color of sol. For instance, the method [194] uses a trypsin conjugate of colloidal gold and consists in recording the interaction of the peptolytic enzyme adsorbed to gold nanoparticles and the protein in solution.

In 1980, Leuvering et al. [195] proposed a new immunoassay method they called the "sol particle immunoassay" (SPIA). A biospecific reaction between target and probe molecules on the colloidal-particle surface results in gold particle aggregation leading to substantial changes in the absorption spectrum, with a noticeable color change from red to blue or gray. It is possible to use the widely available spectrophotometers and colorimeters to assess the reaction outcome. Leuvering et al. [196] also optimized the SPIA by using larger sized gold particles and monoclonal antibodies to various antigenic sites, to detect. Later, the SPIA was used to determine chorionic gonadotropin in the urine of pregnant women, *Rubella* and *Schistosoma* antigens, affinity constants for various isotypes of monoclonal IgG, immunoglobulins in the blood serum of HIV patients, and cystatin C—an endogenous marker for the glomerular filtration rate. The relevant references can be found in [194]. In 2002, Thanh and Rosenzweig [197] "reinvented" this method for determination of anti-protein A with protein A–colloidal gold conjugates.

In some SPIA experiments, despite the obvious complementarity of the molecular probe-target pair, there were no changes in the solution color. It was suggested that a second protein layer is possibly formed on gold particles without loss of the aggregative stability of the sol [194]. Although the spectral changes induced by the adsorption of biopolymers onto metallic particles are relatively small, Englebienne et al. [198] successfully used this approach to develop a quantitative analysis in biomedical applications.

Mirkin et al. [178] proposed a novel SPIA variant, which is based on the colorimetric determination of polynucleotides during their interaction with colloidal-gold particles conjugated through mercaptoalkyls to oligonucleotides of a specific sequence. An alternative variant of DNA-based SPIA without cross-linking interactions was developed by Maeda et al. (see, e.g., recent work [199] and references therein). The colorimetric detection of target DNA with using aggregation phenomena was also developed by Baptista [9] and Rothberg [200] groups. The first approach [9] is based on aggregation of single-strained DNA conjugates (negative reaction) after addition of salt, while the red color of a positive sample (particles covered by

double strained DNA after positive hybridization) remains unchanged. This method was recently efficiently applied for diagnostics of tuberculosis by using samples taken from patients after one stage of PCR [9]. The second approach [200] uses the fact that under certain conditions, single-stranded DNA adsorbs to negatively charged gold nanoparticles in a colloid whereas double-stranded DNA does not. Accordingly, these phenomena determine the colloid stability and color.

A single-analyte bio-barcode assay, as introduced by Mirkin et al. [201], is carried out in a disposable chip through several basic steps [64]. In step 1 the solution with target molecules (TM) sample is mixed with magnetic spheres (MS) conjugated to antibodies and introduced into the separation area of the chip. In step 2 the MS are separated from unreacted molecules by applying a magnetic field and washing. In step 3 gold NPs conjugated to antibodies and double stranded DNA barcodes are introduced into chip and mixed with MS. Bound TMs are sandwiched between the MS and gold NPs, while unbound NPs are washed. In step 4 the MS are retained in the chip and DNA barcodes are dehybridised from them by running water. In step 5 released barcodes are sandwiched between gold NPs and immobilized capture probes. After enhancement with silver and separation from fluidics, the chip is used for an imaging procedure. A multiplexed biobarcode assay is similar to the single analyte assay except for the DNA barcodes are resolved with a 2D array of capture probes before silver enhancement and detection [64].

Along with the extinction-spectrum changes, the particle aggregation is accompanied by the corresponding variation in scattering [202,203]. This phenomenon has been widely used as an analytical tool for determination of various substances in solution. With some methodical cautions [204], it is possible to use commercial spectro-fluorimeters for resonance scattering measurements (see, e.g., [205,206] and references therein).

Due to the more than 100-fold enhancement in quantum yield [106], Au QDs can find interesting applications in biosensorics. For example, Leblanc et al. [207] showed that conjugates of Au_8 QDs with goat-derived anti-human IgG were able to detect human IgG by linear fluorescence quenching.

4.3. Solid-phase assays with nanoparticle markers

A most widespread method for the visualization of biospecific interactions is the solid-phase assay [208], in which the target molecules or antigens are adsorbed on a solid carrier and then revealed with various labels conjugated to recognizing probing molecules, e.g., antibodies (Fig. 23a). Among the diverse solid-phase assay techniques, a special place is occupied by the dot assay, based on the specific staining of a sample drop adsorbed on a membrane [2] or on another substrate. The chief advantage of this method is the possibility of conducting tests without using expensive equipment or means of signal processing. Contrary to, e.g., solid-phase assays using scanning atomic-force microscopy [209], laser-

induced scattering around a nanoabsorber (LISNA) [210], or single-particle resonant-light-scattering spectroscopy [211], such tests may be run under home or field conditions. Examples include known tests for early pregnancy and for narcotic substances or toxins in human blood.

In the dot assay, minimal volumes of target-molecule solutions are applied to a substrate as a series of spots, thus making it possible to perform much more analyzes with the same reagent amounts than, e.g., in the ELISA assay. The sorbent most popular for solid-phase membrane immunoassays is nitrocellulose and modifications thereof [2], although the recent years have also seen the use of siliconized matrices [212] and functionalized-glass microarrays [213], which may be constructed in the form of biochips [214].

At the visualization stage, the membrane is placed in a solution of recognizing molecules conjugated to molecular or corpuscular labels. The conjugates interact with the sample only if complementary target molecules have been adsorbed on the membrane. For detection of biospecific interactions, wide use has been made of such labels as radioactive isotopes, enzymes, and fluorescent dyes. In 1984, several research teams independently proposed using CG as a label in the solid-phase immunoassay [215], in which the intense red color of the marker allows visual determination of the assay results. Information on the principles, technology, and biomedical applications of the immunogold dot assay is detailed in review [2].

In the past few years, the sensitivity of the dot assay using functionalized gold NPs and silver enhancement [8] has been increased down to 1 pg of IgG molecules immobilized on glass or 2.75 ng/ml IgG molecules in solution [216]. There are record-breaking data on the atto- and zeptomolar sensitivity of solid-phase assays [217] (comparable with the sensitivity of resonance scattering [211]) and on the further development of the assay by various means, including the combined use of plasmon-resonant NPs and enzymes [218,219], peptides [220], fluorescent labels [221], and chitosans [222], as well as the use of gold particles with magnetic cores, showing a sensitivity limit of about 0.14 ng/ml [223].

Despite the obvious progress in further developing the dot assay by using metallic NPs, we believe that the method's potential has not yet been fulfilled—first of all, in respect to improving its reliability and sensitivity yet keeping the simplicity of the original one-step procedure (without silver enhancement or other means). The current state of the technology used for synthesizing NPs with specified geometrical and optical parameters offers a multitude of possibilities for optimization of solid-phase analytical technologies. Recent, more detailed studies [224,225] showed that the replacement of colloidal gold conjugates by nanoshells improved the analysis sensitivity to 0.2 ng in the case of nanoshells of sizes 180/15 nm (Fig. 23b) and to 0.4 ng for nanoshells of sizes 100/15 and 140/15 nm. An important question arising with the use of various nanoparticles in the dot immunoassay is as follows: What controls the sensitivity limits of the particle-labeled dot immunoassays? By using the developed theory [225], we explained the dependences of the
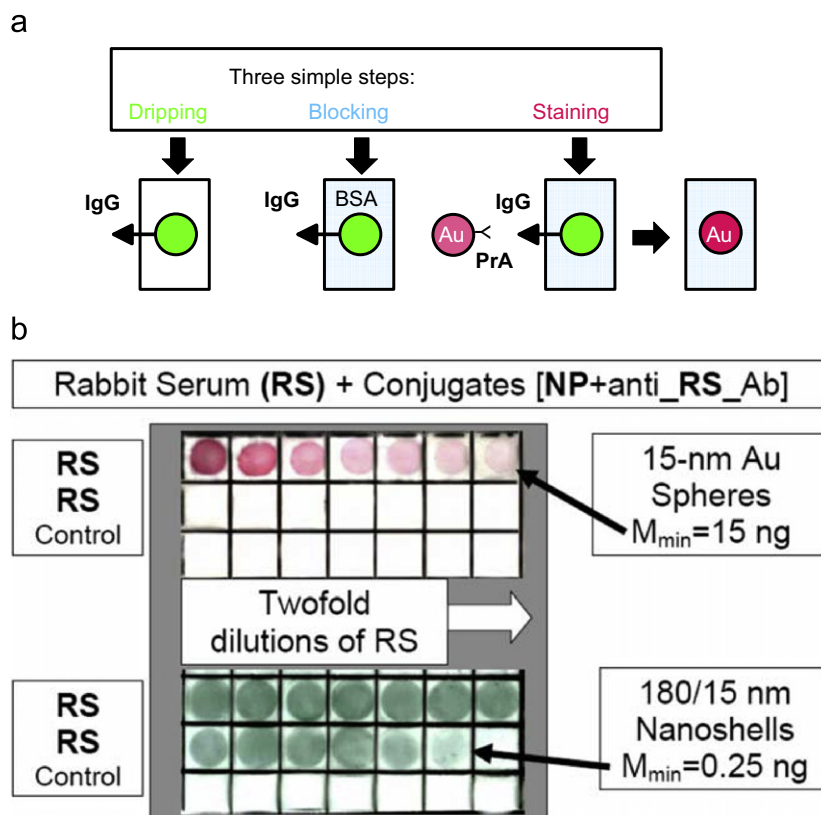
Fig. 23. (a): Basic principles of dot immunoassay include three simple steps: placement of an analyte drop on a membrane strip, blocking of free space with BSA solution, and staining of adsorbed target molecules with biospecific CG conjugates. Here, the target and probing molecules are IgG and protein A, respectively. (b): Dot immunoassays of a normal rabbit serum (RS) by using conjugates of 15 nm colloidal gold particles and silica/gold nanoshells (180/15 nm) with sheep's antirabbit antibodies [225]. The IgG quantity equals 1 μg for the first (upper left) square and is decreased by twofold dilution (left to right). The bottom row of each assay corresponds to a negative control (10 μg BSA in each square).

detection threshold, the sensitivity range of the method, the maximum staining, and the probe-amount saturation threshold on the parameters of particles.

Along with dot immunoassay, NP markers can be used in such solid-phase technologies as immunochromatography and multiplexed lateral flow devices (MLFD) based on gold NPs [2,64]. In particular, MLFD have been successfully applied for simultaneous detection of up to four cardiac markers, parallel detection of up to five threat agents, and serial detection of up to six amplified nucleic acid targets [64].

4.4. Functionalized NPs in biomedical sensing and imaging

Because of sensitivity of PR to the local dielectric environment, plasmonic nanoparticles can act as transducers that convert small changes in the local refractive index into spectral shifts in the extinction and scattering spectra. As a rule, biomolecules have a higher refractive index than buffer solution. Therefore, when a target molecule bind to the nanoparticles surface, the local refractive index increases and the PR wavelength shits to the red. Actually, it is the phenomenon that defines the basic principle of all chemical and biosensors utilizing PR shift as an initial input signal. With this principle,

molecular binding can be monitored in real time with high sensitivity by using transmission or resonance scattering spectrometry.

The first studies of biopolymer adsorption on the CG nanoparticle surface and related optical effects [226,227] showed that the biopolymer binding results in small increase in the extinction and scattering maxima (about 10–20%) and in red-shifting of PR wavelength over 1–20 nm range. Because of the local electrodynamic nature of PR shifting, it is clear that the sensing sensitivity should be dependent on the particle size, shape, and structure. For instance, the problem of sensitivity of CG particles to the local refractive index was formulated as a size-dependent optimization problem which solution revealed the existence of optimal diameters about 30–40 nm for silver and 60–80 nm for gold [172]. Furthermore, the first theoretical studies revealed significant differences between such nanostructures as gold spheres, rods, bispheres, and nanoshells [228,229]. Resent experimental information about the shape-dependent sensitivity of PR to the dielectric environment and relevant references can be found in review [62] and paper [230].

In contrast to ensemble experiments, the single-particle measurements possess potentially much greater sensitivity. Indeed, the single-particle PR shift is caused by

molecules adsorbed on their surface. Typically, the number of adsorbed molecules is less than 100–200, or even smaller. This means that the PR sensitivity of a single PR particle can be about one zeptomole [211]. Recently, Chilkoti et al. [231] presented an analytical model for the rational design of a biosensor based on measuring small PR-shifts of individual gold nanoparticles. The model predicts a minimal detection limit of 18 streptavidin molecules for single-particle sensor, which is in good agreement with experiments and estimates. Moreover, the authors [231] estimated a possible enhancement factor which could potentially provide an 800-fold improvement over the 18 molecule detection limit described in their experimental study. Thus, the ultimate limit of label-free detection of single molecule binding events could be theoretically possible. To conclude this topic, we note that the same idea can be used for a subtle tracking of molecular interaction. For instance, Sönnichsen group [232] demonstrated the ability of probing protein-membrane interaction based on membrane coated plasmonic particles.

The resonance scattering of PR NPs and their bright colors in dark-filed microscopy determine many emerging applications in biomedical imaging. Depending on their size, shape, composition, degree of aggregation, and nature of the stabilizing shell on their surface, PR nanoparticles can appear red, blue and other colors and emit bright resonance light scattering of various wavelengths [233]. To give some quantitative estimation and comparison [62], it is sufficient to note that a single 80 nm silver nanosphere scatters 445 nm blue light with a scattering cross-section of $3 \times 10^4 \, nm^2$, a million fold greater than the fluorescence cross-section of a fluorescein molecule, and a 1000-fold greater than the cross-section of a similarly sized nanosphere filled with fluorescein to the self-quenching limit. Schultz [234] summarized earlier efforts in labeling of cells with NPs.

To illustrate recent advances in NP-based imaging, we restrict our consideration by only few examples. In first experiments, El-Sayed [235,236] and Halas [237] groups demonstrated SPR imaging of cancer cells by using 35 nm CG, gold NRs and NSs conjugated with antibodies to the molecular cancer markers over-expressed on the cell surface. Sokolov et al. used "stellated" particles and polarization-sensitive technique for visualization of molecular cancer cell markers [14]. Recently, Prasad et al. described [238] a multiplex dark-filed microscopy imaging of cancer cells (MiaPaCa) with functionalized Ag and Au nanospheres and gold NRs, that exhibit blue, green, and red scattering colors, respectively.

After publication of first reports [235,237], many research groups were focused on studies of NP conjugates in relation to the cancer diagnostics and therapy. Conjugates of gold NPs with biospecific antibodies to the cancer cell receptors can be used to fabricate high-performance probes for detection of live cancer cell. For example, Yang et al. [239] showed that the conjugate of Cetuximab with Au NP-deposited substrate could detect EGFR-high expressed A431 cells related to epithelial cancer with 54-times larger specificity and sensitivity in comparison with EGFR-deficient MCF7 cells. The thiolated

PEGs as bifunctional cross-linkers can be used for biospecific functionalization of gold NPs with antibodies to the surface cancer cell receptors. Typical example is recent report [240] where 15 nm CG NPs were conjugated via carboxy-terminated PEG dithiol with F19 monoclonal antibodies. These humanized murine antibodies are directed against fibroblast activation protein (FAP-α) which is a serine protease produced specifically by activated fibroblasts. Another example [241] demonstrates the use of PEG-SH to obscure gold nanorods against the reticuloendothelial system in the living organism, whereas the biospecific conjugation were performed by covalent attachment of Herceptin (HER) through Nanothinks acid16 (Sigma-Aldrich). Herceptin is a monoclonal antibody that enables molecular recognition of breast cancer cells expressing highly specific tumor associated antigens. Accordingly, the fabricated conjugates were used for *in vivo* molecular targeting of breast cancer cells.

Although the surface functionalization is typical in biomedical applications of NPs, the "naked" particles themselves may affect biological responses and properties. This topic has been reviewed thoroughly by Bhattacharya and Mukherjee [57].

Besides of PR resonance scattering, a photoacoustic technique were recently developed to monitor systemic circulation of single-particles [17] or their accumulation and aggregation within cells (e.g., within macrophages in atherosclerotic plaques [242]). The method is based on generation of acoustic waves upon pulsed heating of particles, which allows the acoustic monitoring of the particle location or movement.

Another approach utilizes two-photon luminescence (TPL) technique which possesses an obvious advantage over usual dark-field microscopy because of selective excitation of only target particles. This method excludes elastic scattering from nonresonant impurities and it has been successfully applied to visualization of various cells by using CG NPs, NRs, and NSs (see, e.g., [243] and review [21]). The physics behind TPL can be described as follows [21]. The first photon excites an electron through interband transition from sp conduction band below the Fermi level to the sp band above the Fermi level and forms a hole in the first band. The second photon excites a d-electron to the lower sp band, where the first photon has formed the hole. This transition is polarization-dependent and it is efficient for nanorods only in the case of longitudinal polarization. The second photon excites a d-electron to the lower sp band, where the first photon has created the hole. After recombination of the electron and hole, a luminescence photon is emitted.

The combination of TPL with confocal microscopy gives the unique possibility to observe and distinguish PR labels on the surface of and inside cells. It was shown recently that the single-particle resonance TPL intensity of nanorods [243] and nanoshells [16] is sufficient to using these labels as contrast agents for the visualization of cancer molecular markers and investigations of intracellular processes. Moreover, it has been previously shown [244] that usual functionalized CG NPs could be used for the TPL

visualization of particles on the surface of and inside cancer cells.

Discovered 30-years ago, SERS is now one of the potentially power techniques to probe single-molecule interactions [245]. Due to its physical nature, SERS is strongly related to plasmonics, which encompasses and profits from the optical enhancement found in PR NPs and clusters. There have been published a lot of papers on various aspects of SERS, from physical background to medical applications. As starting points, we recommend a couple of recent papers on analytical [246] and biomedical [247] applications of SERS and SEIRA [248].

4.5. Interaction of NPs with living cells and organisms: cell-uptake, biodistribution, and toxicity aspects

The current developments in nanobiotechnology involve the interaction of PR NPs with living organisms, mostly on the cellular and subcellular levels. Given the breadth of currently arising biomedical applications of NPs, it is of great importance to develop an understanding of the complex processes that govern their cellular uptake and intracellular fate, biodistribution over organs of a living organism, and concerns associated with the toxicology of NPs, which is still in its infancy.

Studies on the interface between the parameters of NPs and cell biology are just beginning and a great deal is unknown about the interaction of NPs with cells and organisms and the potential toxicity which may result. The cellular uptake seems to be first important step, which may be affected by the particle geometry (size, shape, etc.) and its surface chemistry. In a series of work (see, e.g., [249,250] and references therein), Chan et al. discovered crucial role of the particle size in the efficiency of cancer cell uptake. Specifically, they showed that gold NPs conjugated with antibodies can regulate the size-dependent processes of binding and activation of membrane receptors, their internalization and subsequent protein expression. It has been found that 40 and 50 nm particles altered signaling processes most effectively, while other particles within 2–100 nm size range also demonstrated measurable effects. These finding means that gold NPs can play an active role in mediating of cellular response rather than serve as inert carriers. Note that Zhang et al. [251] published recently somewhat different observation. Namely, they found that the 20 nm Au NPs coated with TA-terminated PEG5000 showed significantly higher tumor uptake and extravasation from the tumor blood vessels than did the 40 and 80 nm Au NPs. Another approach to the same NR toxicity problem has been recently reported by Parab et al. [252]. In that work, surface modification of CTAB-stabilized gold NRs was carried out by using poly(styrenesulfonate) (PSS) to reduce the toxicity of as-prepared samples because of free CTAB. Electrophoretic measurements confirmed charge reversal due to PSS coating. Functionalization of NRs with PSS significantly increased the cell viability and showed easy intracellular uptake of the nanorods, which suggests their possible use for different biomedical applications.

The surface chemistry is second key factor determining the cellular uptake efficiency. It is generally believed that nanoparticles will remain in the endosome created by the endocytosis process, unless they are microinjected or brought into the cell mechanically. However, it was demonstrated that this endosomal route of cellular uptake can be bypassed by surface modification of the nanoparticles with so-called cell penetrating peptides (CPPs, e.g., CALNN) [253]. Furthermore, successful nuclear targeting was demonstrated using surface modification of NPs with a cocktail of CPPs and a peptide acting as a nuclear localization signal. In the same line, Chan group [254] used several layer-by-layer polyelectrolyte coating to tune the mammalian cellular uptake of gold nanorods from very high to very low by manipulating the surface charge and functional groups of polyelectrolytes. Some peptide motif's are known to deliver a "cargo" into chosen cellular location specifically. Mandal et al. [255] attempted to use this property by modifying gold NPs in order to deliver the particles into osteosarcoma cells through chemical cross-linking with different peptides known to carry protein into cells. Enhanced cellular uptake and anti-cancer efficiency was also reported for conjugates of gold NPs with a dodecylcysteine surfactant [256]. Finally, we note that functionalization of gold NPs with oligonucleotides also was shown to increase the cellular uptake efficiency [257].

Some biomolecules are known to be efficient substances for cellular uptake (e.g., transferrin). Thus, a possible way for design of an efficient nano-vector is to attach these molecules to the NP surface. Yang et al. described an attractive approach to use transferring-conjugated gold NPs as vehicles for specific uptake and targeted drug-delivery [258].

Gold nanoparticles are also being actively used in DNA vaccination [259] and in the *in vivo* preparation of antibodies specific to complete antigens and various haptens [260]. When serving as an antigen carrier, CG enhances the phagocytic activity of macrophages and exerts an influence on lymphocyte functioning; this fact possibly determines the immunomodulating effect of CG. The most interesting aspect of manifestation of immunogenic properties by hapten after immobilization on CG is that gold nanoparticles serve as both a carrier and an adjuvant—that is, they present the hapten to T cells in some way. Several authors reported on responses of Kupffer cells [261] and peritoneal macrophages [262] during interaction with gold nanoparticles. Vallhov et al. [263] discussed the influence of dendritic cells on the formation of an immune response upon administration of an antigen conjugated to gold nanoparticles.

Pharmacokinetic and organ/tissue distribution properties of functionalized NPs are of great interest from clinical point of view because of potential human cancer treatment. After the initial injection of NPs into animal, the systemic circulation distributes the NPs towards all organs in the body. Several publications have shown distribution of NPs to multiple animal organs including spleen, heart, liver, and brain. For instance, Hillyer and Albrecht [264] observed an increased distribution to other organs after oral administration of gold NPs of decreasing

size (from 58 to 4 nm) to mice. The highest amount of CG NPs was obtained for smallest particles (4 nm) administered orally. For 13 nm CG NPs, the highest amount of gold was detected in liver and spleen after intraperitoneal administration [264]. Niidome et al. [265] showed that after intravenously injection of gold NRs these particles accumulated predominantly in the liver within 30 min. The coating of gold NRs by PEG-thiols resulted in a prolonged circulation.

De Jong et al. [266] performed a kinetic study to evaluate the gold NPs size (10, 50, 100 and 250 nm) effects on the *in vivo* tissue distribution of NPs in the rat. Rats were intravenously injected in the tail vein with gold NPs and the gold particle distribution was measured quantitatively 24 h after injection. The authors showed that the tissue distribution of gold NPs is size-dependent with the smallest 10 nm NPs possessing the most widespread organ distribution. Analogous study for 1.4 and 18 nm gold NPs was reported by Semmler-Behnke et al. [267] for biodistribution in rats and by Zhang et al. [251] for biodistribution of 20, 40, and 80 nm Au NPs in nude mice.

Katti et al. [268] published detailed *in vitro* analysis and *in vivo* pharmacokinetics studies of gold NPs within the nontoxic phytochemical gum arabic matrix in pigs to gain insight into the organ-specific localization. Pigs were chosen as excellent animal models because of their similar physiological and anatomical characteristics to those of human beings. Kogan et al. reported data on biodistribution of PEG-coated 15×50 nm gold NRs and 130 nm silica/gold NSs in tumor-bearing mice [269]. The kinetic of gold distribution was evaluated for blood, liver, tumor, and muscles over 1 h (NRs) and 24 h (NSs) periods. It was found that the gold NRs were non-specifically accumulated in tumors with significant contrast in comparison with other organs, while silica/gold NSs demonstrated more smooth distribution. This study was recently extended in our report [270], where kinetics, biodistribution, and histological examinations were performed to evaluate the particle-size effects on distribution of 15 and 50 nm PEG-coated CG particles and 160 nm silica/gold NSs in the rats and rabbits. The above NPs were used as model because of their importance for current biomedical applications such as the photothermal therapy, the optical coherence tomography, and the resonance-scattering imaging. The dynamics of NPs circulation *in vivo* was evaluated after intravenous administration of 15 nm CG NPs to rabbit, and the maximal concentrations of gold were observed 15–30 min after injection. Rats were injected in the tail vein with PEG-coated NPs (about 0.3 mg Au/kg rats). 24 h after injection, the accumulation of gold in different organs and blood was determined by the atomic absorption spectroscopy. In accordance with the published reports, we observed 15 nm particles in all organs with rather smooth distribution over liver, spleen and blood (Fig. 24). By contrast, the larger NSs were accumulated mainly in liver and spleen. For rabbits, the biodistribution was similar (72 h after intravenous injection).

Though NPs has been estimated to increase from 2300 tons produced today to 58 000 tons by 2020 [271], the current knowledge on the NPs toxicity effects is quite
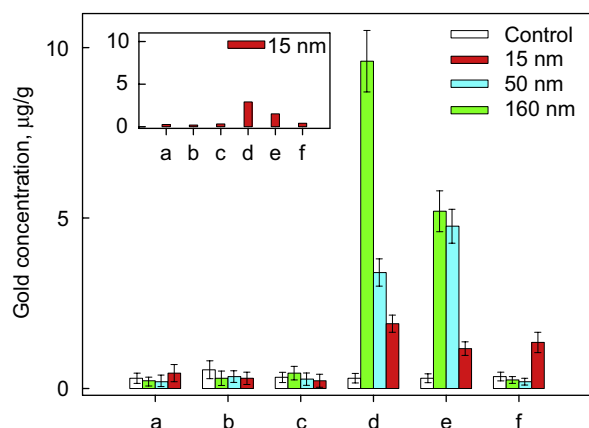

Fig. 24. Au concentrations in rat organs 24 h after intravenous administration of 15, 50, and 160 nm NPs. a—brain, b—kidney, c—lung, d—liver, e—spleen, f—blood [270]. The insert shows the biodistribution of 15 nm gold NPs 72 h after injection in rabbit. The bars show standard errors of the mean.

limited and also reported results are confusing (see, e.g., citations in Ref. [271]). Despite the great excitement about the potential uses of gold nanoparticles for medical diagnostics, as tracers, and for other biological applications, researchers are increasingly aware that potential NP toxicity must be investigated before any *in vivo* applications of gold nanoparticles can move forward.

At present, it would be quite desirable to separate the toxicity effects related to the particles themselves and to their surface coatings. For example, Chan group [254] found that CTAB-coated rods did not produce significant toxicity in media containing serum. This finding suggests that serum proteins bind to nanorods and shield the toxic surface coating. On the other hand, Ray et al. [271] reported high toxicity of CTAB-coated NR. A close inspection of their data suggests that the reported toxicity was due to desorption of CTAB molecules. Note, that the reported [271] toxicity of usual CG NPs was very small in accord with recent study of biocompatibility of 5, 15, and 30 nm CG NPs [272]. The importance of surface chemistry and cell type for interpretation of nanoparticle cytotoxicity studies also has been recently illustrated by Murphy et al. [273].

For more detailed consideration of the NP toxicity, the readers are referred to recent reviews [60,274] (general consideration of various NPs) and [55,273] (gold NPs). Recent review [275] presents a detailed summary of the in vitro cytotoxicity data currently available on three classes of NPs: carbon-based NPs (such as fullerenes and nanotubes), metal-based NPs (such as CG NPs, NSs, and NRs), and semiconductor-based NPs (such as quantum dots).

4.6. Application of NPs to drug delivery and photothermal therapy

The surface functionalization of NPs and their cellular uptake are closely related to the targeted drug delivery problems. Gold NPs have recently considered as a
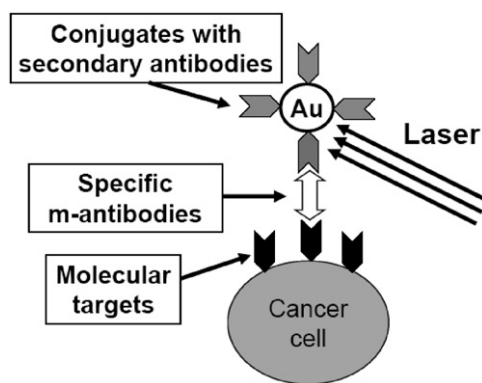
Fig. 25. Scheme of PTT therapy. In step 1, the molecular cancer targets (MCT, e.g., EGFR) are labeled with primary monoclonal specific antibodies. In step 2, these m-antibodies are sandwiched between MCT and gold NPs conjugated with secondary antibodies. In step 3, irradiation with a laser pulse results in drastic heating of NPs and cancer cell death.

promising candidate for delivery of small drug molecules or large biomolecules into their targets [13,57]. Owing to their inherent properties such us tunable size and low polydispersity, long-term stability and weak toxicity, easy functionalization and large surface-to-volume ratio gold NPs could find promising application in the drug delivery technologies [276]. Efficient release of these therapeutic agents could be triggered by internal or external stimuli. In the case of cancer therapy, CG NPs also could be used as a platform for developing multifunctional tumor-targeted drug delivery vectors [277]. For example, Patra et al. described recently an efficient application of 5 nm gold Ns conjugated with anti-EGFR antibodies Cetuximab (C225) and Gemcitabine for targeted delivery of Gemcitabine to pancreatic adenocarcinoma [278].

Targeted delivery of conjugated NPs could improve the therapeutic efficiency of known technologies as photodynamic therapy [279] and new emerged field called plasmonic photothermal therapy (PPTT) [11]. In 2003, nanoshell-based therapy was first demonstrated in tumors grown in mice by Halas et al. [280], while Pitsillides et al. [281] and El-Sayed et al. [236] published first application of CG NPs and gold NR for PPTT *in vitro*. Basic principles of PPTT are explained in Fig. 25.

As the available hyperthermic techniques for cancer tumor therapy [282] possess low spatial selectivity in heating of tumor and surrounding healthy tissues, one of the ways to improve the laser heating spatial selectivity is the labeling of tumor with PR NPs. By exposing NPs to laser radiation near their plasmon-resonant absorption band, it is possible to produce local heating of labeled cancer cells without harming surrounding healthy tissues. The spectral tuning of nanoparticle resonance to the "therapeutic optical window" (750–1100 nm) and getting the desired ratio between the absorption and scattering efficiencies can be achieved by variation in the particle size, shape and structure [140].

A first step in enhancement of the PPTT efficiency is clear understanding of the relationship between the nanoparticle/cluster parameters (size, shape, particle/cluster structure, etc.) and optical responses. We reported

[140] theoretical simulations aimed at finding the optimal single-particle and cluster structures to achieve its maximal absorption which is crucial for PT therapeutic effects. To characterize the optical amplification in laser-induced thermal effects, it is convenient to introduce relevant parameters such as the ratio of the absorption cross section to the gold mass of a single-particle structure and absorption amplification, defined as the ratio of cluster absorption to the total absorption of noninteracting particles. We have simulated the absorption efficiency of single nanoparticles (gold spheres, rods, and silica/gold nanoshells), linear chains, 2D lattice arrays, 3D random volume clusters, and the random aggregated *N*-particle ensembles on the outer surface of a larger dielectric sphere, which mimic aggregation of nanosphere bioconjugates on or within cancer cells. The clusters particles are bare or biopolymer-coated gold nanospheres. The light absorption of cluster structures is studied by using the generalized multiparticle Mie solution and the T-matrix method. The gold nanoshells with (silica core diameter)/(gold shell thickness) parameters of $(50-100)/(3-8)$ nm and nanorods with minor/major sizes of $(15-20)/(50-70)$ nm are shown to be more efficient PT labels and sensitizers than the equivolume solid single gold spheres. In the case of nanosphere clusters, the interparticle separations and the short linear-chain fragments are the main structural parameters determining the absorption efficiency and its spectral shifting to the red. Although we have not found a noticeable dependence of absorption amplification on the cluster sphere size, 20–40 nm particles are found to be most effective, in accord with our experimental observations. The long-wavelength absorption efficiency of random clusters increases with the cluster particle number *N* at small *N* and reveals a saturation behavior at $N > 20$. Besides the linear optical responses, the second important point is related to the modeling of the heat transfer processes. This question has been addressed in several previous reports (see, e.g., Ref. in [140]) and in a recent work [283].

Among great variety of possible nanoparticle PPTT platforms, gold nanoshells seem to be a promising candidate because of robust fabrication and functionalization protocols and significant absorption cross section. Halas et al. [12] recently reviewed the properties of nanoshells that are relevant to their preparation and use in cancer diagnostics and therapy. It was stressed that specific functionalization technologies are necessary for both passive uptake of nanoshells into tumors and for targeting specific cell types. NS based PPTT in several animal models of human tumors have produced highly promising results, and the corresponding NP dosage information, thermal response, and tumor outcomes for these experiments can be found in Ref. [12].

Although several preclinical reports on the utility of gold NSs for PPTT and OCT applications are available [12], there are remain several areas still to be studied more thoroughly. First of all the question is about controlled and localized hyperthermia without significant overheating of both tumor and surrounding normal tissues. A resent report [284] describes the investigation of heating kinetics, spatial temperature distribution, and morpholo-

gical alterations in tissues dependent on laser irradiation parameters and nanoparticle concentration. The experimental results for phantoms and laboratory animals at several temperature regimes and related morphological tissue patterns were also considered. We anticipate that additional research and theoretical models achievable temperature elevations are needed to apply PPTT as generally as possible to tumor remission. There is a need for effective quantification methods for accumulation of NPs in tumors.

In the future development of PPTT technologies, one needs to address a number of variables, e.g., stability, biocompatibility, and chemical reactions of nanoparticles bioconjugates in physiological environments, blood retention time, tumor extravasation, the fate of the nanoparticles following therapy, etc. [11]. Most of the published *in vivo* studies have been carried out for subcutaneous tumors easily accessible to NIR light applied over the skin. For convenient clinical applications of PPTT one needs to deliver NIR light deep into tissue by exploiting fiber optic probes or other means.

5. Conclusion

In this review, we have discussed the chemistry-based bottom-up protocols for fabrication of particles with the desired size, shape, and structure. In the case of silver NPs, however, there remain some problems related with NP stability and the synthetic protocol reproducibility. Our own expertize and communications from colleagues reveal rather poor reproducibility of polyol protocols for silver nanocube or nanocages fabrication.

The geometrical and structural parameters of NPs determine the individual linear optical properties, which can now be characterized at the single-particle level. The main effort now should be directed to improve the single-particle imaging techniques and the signal-to-noise ratio. Current development of the electromagnetic simulation tools allows for modeling various complex assemblies of bare or functionalized metal NPs.

For biomedical applications, the surface functionalization of NPs with biospecific molecules is crucial step which determines following properties of conjugates and the overall success of applied technologies. Although significant progress has seen over last 5-years, there are evident needs in development of simple and robust protocols. In particular, such protocols are needed for Au and Au–Ag NRs.

Recent publications on carbon nanotubes injected into mice and resulting in mesotheliom [12] clearly demonstrate that the toxicity concerns need to be addressed in a serious and systematic way. Every novel application of nanotechnology for the detection, imaging, drug delivery or therapeutic treatment should takes into account all potential toxicities, both those to the patient and those to the environment.

Because of the daily updated list of publications on PR particles, this review is necessarily incomplete and should be considered as a starting point for understanding basic principles behind NP fabrication, plasmonic properties,

and biomedical applications. We conclude the review by citation of two papers published in the January issue of Nature, 2008, which are devoted to the fabrication of artificial single crystals with use of gold NPs-oligonucleotide conjugates as building blocks [285,286]. These publications are quite symbolic. First, the two research groups have simultaneously obtained a sounding result. Second, this demonstrates again the exciting possibilities of nanobiotechnology and biophotonics based on the use of new building PR particle-molecule blocks.

References

[1] Boisselier E, Astruc D. Gold nanoparticles in nanomedicine: preparations, imaging, diagnostics, therapies and toxicity. Chem Rev 2009;38:1759–82.

[2] Dykman LA, Bogatyrev VA. Gold nanoparticles: preparation, functionalisation and applications in biochemistry and immunochemistry. Russ Chem Rev 2007;76:181–94.

[3] Shim S-Y, Lim D-K, Nam J-M. Ultrasensitive optical biodiagnostic methods using metallic nanoparticles. Nanomedicine 2008;3:215–32.

[4] Panyala1 NR, Pena-Mendez EM, Havel J. Gold and nano-gold in medicine: overview, toxicology and perspectives. J Appl Biomed 2009;7:75–91.

[5] Kreibig U, Vollmer M. Optical properties of metal clusters. Berlin: Springer; 1995.

[6] Liu X, Dai Q, Austin L, Coutts J, Knowles G, Zou J, et al. Homogeneous immunoassay for cancer biomarker detection using gold nanoparticle probes coupled with dynamic light scattering. J Am Chem Soc 2008;130:2780–2.

[7] Stewart ME, Anderton CR, Thompson LB, Maria J, Gray SK, Rogers JA, et al. Nanostructured plasmonic sensors. Chem Rev 2008;108:494–521.

[8] Gupta S, Huda S, Kilpatrick PK, Velev OD. Characterization and optimization of gold nanoparticle-based silver-enhanced immunoassays. Anal Chem 2007;79:3810–20.

[9] Baptista P, Pereira E, Eaton P, Doria G, Miranda A, Gomes I, et al. Gold nanoparticles for the development of clinical diagnosis methods. Anal Bioanal Chem 2008;391:943–50.

[10] Luo PG, Stutzenberger FJ. Nanotechnology in the detection and control of microorganisms. Adv Appl Microbiol 2008;63:145–81.

[11] Huang X, Jain PK, El-Sayed IH, El-Sayed MA. Plasmonic photo-thermal therapy (PPTT) using gold nanoparticles. Lasers Med Sci 2008;23:217–28.

[12] Lal S, Clare SE, Halas NJ. Nanoshell-enabled photothermal cancer therapy: impending clinical impact. Acc Chem Res 2008;41:1842–51.

[13] Han G, Ghosh P, Rotello VM. Functionalized gold nanoparticles for drug delivery. Nanomedicine 2007;2:113–23.

[14] Aaron J, de la Rosa E, Travis K, Harrison N, Burt J, José-Yakamán M, et al. Polarization microscopy with stellated gold nanoparticles for robust monitoring of molecular assemblies and single biomolecules. Opt Express 2008;16:2153–67.

[15] Gobin AM, Lee MH, Halas NJ, James WD, Drezek RA, West JL. Near-infrared resonant nanoshells for combined optical imaging and photothermal cancer therapy. Nano Lett 2007;7:1929–34.

[16] Park J, Estrada A, Sharp K, Sang K, Schwartz JA, Smith DK, et al. Two-photon-induced photoluminescence imaging of tumors using near-infrared excited gold nanoshells. Opt Express 2008;16:1590–9.

[17] Zharov V, Galanzha E, Shashkov E, Khlebtsov N, Tuchin V. *In vivo* photoacoustic flow cytometry for monitoring circulating cells and contrast agents. Opt Lett 2006;31:3623–5.

[18] Shalaev VM. Optical negative-index metamaterials. Nat Photon 2007;1:41–8.

[19] Odom TW, Nehl CL. How gold nanoparticles have stayed in the light: the 3M's principle. ACS NANO 2008;2:612–6.

[20] Pelton M, Aizpurua J, Bryant G. Metal-nanoparticle plasmonics. Laser Photon Rev 2008;2:136–59.

[21] Khlebtsov NG. Optics and biophotonics of nanoparticles with a plasmon resonance. Quant Electron 2008;38:504–29.

[22] Daniel MC, Astruc D. Gold nanoparticles: assembly, supramolecular chemistry, quantum–size-related properties, and applications toward biology, catalysis, and nanotechnology. Chem Rev 2004;104:293–346.

[23] Dykman LA, Bogatyrev VA, Shchyogolev SY, Khlebtsov NG. Gold nanoparticles: synthesis, properties, biomedical applications. Moscow: Nauka; 2008 (in Russian).

[24] Pastoriza-Santos I, Liz–Marzán LM. Colloidal silver nanoplates. State of the art and future challenges. J Mater Chem 2008;18:1724–37.

[25] Sun Y, Xia Y. Shape-controlled synthesis of gold and silver nanoparticles. Science 2002;298:2176–9.

[26] Wang H, Brandl DW, Le F, Nordlander P, Halas NJ. Nanorice: a hybrid plasmonic nanostructure. Nano Lett 2006;6:827–32.

[27] Nehl CL, Liao H, Hafner JH. Optical properties of star-shaped gold nanoparticles. Nano Lett 2006;6:683–8.

[28] Sun Y, Xia Y. Alloying and dealloying processes involved in the preparation of metal nanoshells through a galvanic replacement reaction. Nano Lett 2003;3:1569–72.

[29] Rechberger W, Hohenau A, Leitner A, Krenn JR, Lamprecht B, Aussenegg FR. Optical properties of two interacting gold nanoparticles. Opt Commun 2003;220:137–41.

[30] Haynes CL, van Duyne RP. Nanosphere lithography: a versatile nanofabrication tool for studies of size-dependent nanoparticle optics. J Phys Chem B 2001;105:5599–611.

[31] Zhao J, Pinchuk AO, McMahon JM, Li S, Ausman LK, Atkinson AL, et al. Methods for describing the electromagnetic properties of silver and gold nanoparticles. Acc Chem Res 2008;41:1710–20.

[32] Myroshnychenko V, Rodríguez-Fernandez J, Pastoriza-Santos I, Funston AM, Novo C, Mulvaney P, et al. Modelling the optical response of gold nanoparticles. Chem Soc Rev 2008;37:1792–805.

[33] Schultz S, Smith DR, Mock JJ, Schultz DA. Single-target molecule detection with nonbleaching multicolor optical immunolabels. Proc Natl Acad Sci USA 2000;97:996–1001.

[34] Arbouet A, Christofilos D, Del Fatti N, Vallée F, Huntzinger JR, Arnaud L, et al. Direct measurement of the single-metal-cluster optical absorption. Phys Rev Lett 2004;93:127401.

[35] Del Fatti N, Christofilos D, Vallée F. Optical response of a single gold nanoparticles. Gold Bull 2008;41:147–58.

[36] Berciaud S, Cognet L, Tamarat P, Lounis B. Observation of intrinsic size effects in the optical response of individual gold nanoparticles. Nano Lett 2005;5:515–8.

[37] Muskens OL, Del Fatti N, Vallée F, Huntzinger JR, Billaud P, Broyer M. Single metal nanoparticle absorption spectroscopy and optical characterization. Appl Phys Lett 2006;88:0634109.

[38] Klar T, Perner M, Grosse S, von Plessen G, Spirkl W, Feldmann J. Surface-plasmon resonances in single metallic nanoparticles. Phys Rev Lett 1998;80:4249–52.

[39] Glomm WR. Functionalized gold nanoparticles for applications in bionanotechnology. J Disp Sci Technol 2005;26:389–414.

[40] Zhou J, Ralston J, Sedev R, Beattie DA. Functionalized gold nanoparticles: synthesis, structure and colloid stability. J Colloid Interface Sci 2008;331:251–62.

[41] Mitamura K, Imae T. Functionalization of gold nanorods toward their applications. Plasmonics 2009;4:23–30.

[42] Liz-Marzán LM. Tailoring surface plasmons through the morphology and assembly of metal nanoparticles. Langmuir 2006;22:32–41.

[43] Hu M, Chen J, Li Z-Y, Au L, Hartland GV, Li X, et al. Gold nanostructures: engineering their plasmonic properties for biomedical applications. Chem Soc Rev 2006;35:1084–94.

[44] Nehl CL, Hafner JH. Shape-dependent plasmon resonances of gold nanoparticles. J Mater Chem 2008;8:2415–9.

[45] Major KJ, De C, Obare SO. Recent advances in the synthesis of plasmonic bimetallic nanoparticles. Plasmonics 2009;4:61–78.

[46] Tao AR, Habas S, Yang P. Shape control of colloidal metal nanocrystals. Small 2008;4:310–25.

[47] Biju V, Itoh T, Anas A, Sujith A, Ishikawa M. Semiconductor quantum dots and metal nanoparticles: syntheses, optical properties, and biological applications. Anal Bioanal Chem 2008;391:2469–95.

[48] Yang S-M, Kim S-H, Lim J-M, Yi G-R. Synthesis and assembly of structured colloidal particles. J Mater Chem 2008;18:2177–90.

[49] Tréguer-Delapierre M, Majimel J, Mornet S, Duguet E, Ravaine S. Synthesis of non-spherical gold nanoparticles. Gold Bull 2008;41:1195–207.

[50] Olson TY, Zhang JZ. Structural and optical properties and emerging applications of metal nanomaterials. J Mater Sci Technol 2008;24:433–46.

[51] Harris N, Ford MJ, Mulvaney P, Cortie MB. Tunable infrared absorption by metal nanoparticles: the case for gold rods and shells. Gold Bull 2008;41:5–14.

[52] Lal S, Grady NK, Kundu J, Levin CS, Lassiter JB, Halas NJ. Tailoring plasmonic substrates for surface enhanced spectroscopies. Chem Soc Rev 2008;37:898–911.

[53] Zhang JZ, Noguez C. Plasmonic optical properties and applications of metal nanostructures. Plasmonics 2008;3:127–50.

[54] Cheng MM-C, Cuda G, Bunimovich Y, Gaspari M, Heath JR, Hill HD, et al. Nanotechnologies for biomolecular detection and medical diagnostics. Curr Opin Chem Biol 2006;10:11–9.

[55] Brown CL, Whitehouse MW, Tiekink ERT, Bushell GR. Colloidal metallic gold is not bio-inert. Inflammopharmacology 2008;16:133–7.

[56] Roca M, Haes AJ. Probing cells with noble metal nanoparticle aggregates. Nanomedicine 2008;3:555–65.

[57] Bhattacharya R, Mukherjee P. Biological properties of "naked" metal nanoparticles. Adv Drug Deliv Rev 2008;60:1289–306.

[58] Sperling RA, Gil PR, Zhang F, Zanella M, Parak WJ. Biological applications of gold nanoparticles. Chem Soc Rev 2008;37:1896–908.

[59] White KA, Rosi NL. Gold-nanoparticle based assays for the detection of biologically relevant molecules. Nanomedicine 2008;3:543–53.

[60] Stern ST, McNeil SE. Nanotechnology safety concerns revisited. Toxicolog Sci 2008;101:4–21.

[61] Uechi I, Yamada S. Photochemical and analytical applications of gold nanoparticles and nanorods utilizing surface plasmon resonance. Anal Bioanal Chem 2008;391:2411–21.

[62] Anker JN, Hall WP, Lyandres O, Shah NC, Zhao J, van Duyne RP. Biosensing with plasmonic nanosensors. Nat Mater 2008;7:442–53.

[63] Tong L, Wei Q, Wei A, Cheng J-X. Gold nanorods as contrast agents for biological imaging: optical properties, surface conjugation and photothermal effects. Photochem Photobiol 2009;85:21–32.

[64] Wilson R. The use of gold nanoparticles in diagnostics and detection. Chem Soc Rev 2008;37:2028–45.

[65] Homola J. Surface plasmon resonance sensors for detection of chemical and biological species. Chem Rev 2008;108:462–93.

[66] Azzazy HME, Mansour MMH. *In vitro* diagnostic prospects of nanoparticles. Clin Chim Acta 2009:4031–8.

[67] Faraday M. Experimental relations of gold (and others metals) to light. Phil Trans Royal Soc (Lond) 1857;147:145–81.

[68] Zsigmondy R. Üeber wassrige Lösungen metallischen Goldes. Ann Chem 1898;301:29–54.

[69] Mie G. Beitrage zur Optik truber Medien, speziell kolloidaler Metallösungen. Ann Phys 1908;25:377–445.

[70] Svedberg T. The formation of colloids. London: Churchill; 1921.

[71] Turkevich J, Garton G, Stevenson PC. The color of colloidal gold. J Colloid Sci 1954;9(Suppl 1):26–35.

[72] Frens G. Controlled nucleation for the regulation of the particle size in monodisperse gold suspensions. Nature Phys Sci 1973;241:20–2.

[73] Khlebtsov NG, Bogatyrev VA, Dykman LA, Melnikov AG. Spectral extinction of colloidal gold and its biospecific conjugates. J Colloid Interface Sci 1996;180:436–45.

[74] Baschong W, Lucocq JM, Roth J. "Thiocyanate gold": small (2–3 nm) colloidal gold for affinity cytochemical labeling in electron microscopy. Histochemistry 1985;83:409–11.

[75] Brown KR, Walter DG, Natan MJ. Seeding of colloidal au nanoparticle solutions. 2. Improved control of particle size and shape. Chem Mater 2000;12:306–13.

[76] Goia DV, Matijević E. Tailoring the particle size of monodispersed colloidal gold. Coll Surf A 1999;146:139–52.

[77] Gentry ST, Fredericks SJ, Krchnavek R. Controlled particle growth of silver sols through the use of hydroquinone as a selective reducing agent. Langmuir 2009;25:2613–21.

[78] Martin CR. Nanomaterials: a membrane based synthetic approach. Science 1994;266:1961–6.

[79] Yu Y-Y, Chang S-S, Lee C-L, Wang CRC. Gold nanorods: electro-chemical synthesis and optical properties. J Phys Chem B 1997;101:6661–4.

[80] Jana N, Gearheart L, Murphy C. Wet chemical synthesis of high aspect ratio cylindrical gold nanorods. J Phys Chem B 2001;105:4065–7.

[81] Nikoobakht B, El-Sayed MA. Preparation and growth mechanism of gold nanorods (NRs) using seed-mediated growth method. Chem Mater 2003;15:1957–62.

[82] Alekseeva AV, Bogatyrev VA, Dykman LA, Khlebtsov BN, Trachuk LA, Melnikov AG, et al. Preparation and optical scattering characterization of au nanorods, and their application to a dot-immunogold assay. Appl Opt 2005;44:6285–95.

[83] Sharma V, Park K, Srinivasaraoa M. Shape separation of gold nanorods using centrifugation. Proc Natl Acad Sci USA 2009;106:4981–5.

[84] Khanal BP, Zubarev ER. Purification of high aspect ratio gold nanorods: complete removal of platelets. J Am Chem Soc 2008;130:12634–5.

[85] Murphy CJ, Sau TK, Gole AM, Orendorff CJ, Gao J, Gou L, et al. Anisotropic metal nanoparticles: synthesis, assembly, and optical applications. J Phys Chem B 2005;109:13857–70.

[86] Pérez-Juste J, Pastoriza-Santos I, Liz-Marzán LM, Mulvaney P. Gold nanorods: synthesis, characterization and applications. Coord Chem Rev 2005;249:1870–9.

[87] Alekseeva AV, Bogatyrev VA, Khlebtsov BN, Melnikov AG, Dykman LA, Khlebtsov NG. Gold nanorods: synthesis and optical properties. Colloid J 2006;68:661–78.

[88] Ni W, Kou X, Yang Z, Wang J. Tailoring longitudinal surface plasmon wavelengths, scattering and absorption cross sections of gold nanorods. ACS NANO 2008;2:677–86.

[89] Pietrobon B, McEachran M, Kitaev V. Synthesis of size-controlled faceted pentagonal silver nanorods with tunable plasmonic properties and self-assembly of these nanorods. ACS NANO 2009;3:21–6.

[90] Ah CS, Hong SD, Jang D-J. Preparation of $Au_{core}Ag_{shell}$ nanorods and characterization of their surface plasmon resonances. J Phys Chem B 2001;105:7871–3.

[91] Liu M, Guyot-Sionnest P. Synthesis and optical characterization of Au/Ag core/shell nanorods. J Phys Chem B 2004;108:5882–8.

[92] Becker J, Zins I, Jaka A, Khalavka Yu, Schubert O, Sönnichsen C. Plasmonic focusing reduces ensemble linewidth of silver-coated gold nanorods. Nano Lett 2008;8:1719–23.

[93] Oldenburg S, Averitt RD, Westcott S, Halas NJ. Nanoengineering of optical resonances. Chem Phys Lett 1998;288:243–7.

[94] Brinson BE, Lassiter JB, Levin CS, Bardhan R, Mirin N, Halas NJ. Nanoshells made easy: improving Au layer growth on nanoparticle surfaces. Langmuir 2008;24:14166–71.

[95] Phonthammachai N, Kah JCY, Jun G, Sheppard CJR, Olivo MC, Mhaisalkar SG, et al. Synthesis of contiguous silica–gold core-shell structures: critical parameters and processes. Langmuir 2008;24:5109–12.

[96] Shi W, Sahoo Y, Swihart MT, Prasad PN. Gold nanoshells on polystyrene cores for control of surface plasmon resonance. Langmuir 2005;21:1610–7.

[97] Kim J-H, Bryan WW, Lee TR. Preparation, characterization, and optical properties of gold, silver, and gold–silver alloy nanoshells having silica cores. Langmuir 2008;24:11147–52.

[98] Chen D, Liu H-Y, Liu J-S, Ren X-L, Meng X-W, Wu W, et al. A general method for synthesis continuous silver nanoshells on dielectric colloids. Thin Solid Films 2008;516:6371–6.

[99] Ye J, Van Dorpe P, Van Roy W, Borghs G, Maes G. Fabrication, characterization, and optical properties of gold nanobowl sub-monolayer structures. Langmuir 2009;25:1822–7.

[100] Sun Y, Mayers BT, Xia Y. Template-engaged replacement reaction: a one-step approach to the large-scale synthesis of metal nanostructures with hollow interiors. Nano Lett 2002;2:481–5.

[101] Sun Y, Xia Y. Alloying and dealloying processes involved in the preparation of metal nanoshells through a galvanic replacement reaction. Nano Lett 2003;3:1569–72.

[102] Silvert P-Y, Herrera-Urbina R, Duvauchelle N, Vijayakrishnan V, Elhsissen TK. Preparation of colloidal silver dispersions by the polyol process. Part 1—synthesis and characterization. J Mater Chem 1996;6:573–7.

[103] Chen J, McLellan JM, Siekkinen A, Xiong Y, Li Z-Y, Xia Y. Facile synthesis of gold–silver nanocages with controllable pores on the surface. J Am Chem Soc 2006;128:14776–7.

[104] Liu M, Guyot-Sionnest P. Mechanism of silver(I)-assisted growth of gold nanorods and bipyramids. J Phys Chem B 2005;109:22192–200.

[105] Li C, Shuford KL, Chen M, Lee EJ, Cho SO. A facile polyol route to uniform gold octahedra with tailorable size and their optical properties. ACS NANO 2008;2:1760–9.

[106] Zheng J, Petty JT, Dickson RM. High quantum yield blue emission from water-soluble Au_8 nanodots. J Am Chem Soc 2003;125:7780–1.

[107] Huang T, Murray RW. Visible luminescence of water-soluble monolayer-protected gold clusters. J Phys Chem B 2001;105:12498–502.

[108] Palik ED, editor. Handbook of optical constants of solids. New York: Academic Press, Parts I, II, III; 1985, 1991, 1998.

[109] Coronado EA, Schatz GC. Surface plasmon broadening for arbitrary shape nanoparticles: a geometrical probability approach. J Chem Phys 2003;119:3926–34.

[110] Moroz A. Electron mean free path in a spherical shell geometry. J Phys Chem C 2008;112:10641–52.

[111] Bohren CF, Huffman DR. Absorption and scattering of light by small particles. New York: Wiley; 1983.

[112] Rayleigh DW. On the scattering of light by small particles. Phil Mag 1871;41:447–54.

[113] Gans R. Über die Form ultramikroskopischer Goldteilchen. Ann Phys 1912;37:881–900.

[114] Rayleigh DW. On the incidence of aerial and electric waves upon small obstacles in the from of ellipsoids or elliptic cylinders, and on the passage of electric waves through a circular aperture in a conducting screen. Phil Mag 1897;44:28–52.

[115] Draine BT. The discrete dipole approximation for light scattering by irregular targets. In: Mishchenko MI, Hovenier JW, Travis LD, editors. Light scattering by nonspherical particles: theory, mea-surements, and applications. San Diego: Academic Press; 2000. p. 131–45.

[116] Talfove A., editor. Advances in computational electrodynamics: the finite-difference-time-domain method. Artech House, Boston, 1998.

[117] Hafner C. Post-modern electromagnetics: using intelligent Max-well solvers. New York: Wiley; 1999.

[118] Mishchenko MI, Travis LD, Lacis AA. Scattering, absorption, and emission of light by small particles. Cambridge: University Press; 2002.

[119] Link S, El-Sayed MA. Optical properties and ultrafast dynamics of metallic nanocrystals. Annu Rev Phys Chem 2003;54:331–66.

[120] Johnson PB, Christy RW. Optical constants of noble metals. Phys Rev B 1972;6:4370–9.

[121] Oubre C, Nordlander P. Optical properties of metallodielectric nanostructures calculated using the finite difference time domain method. J Phys Chem B 2004;108:17740–7.

[122] Mulvaney P. Surface plasmon spectroscopy of nanosized metal particles. Langmuir 1996;12:788–800.

[123] Persson BNJ. Polarizability of small spherical metal particles: influence of the matrix environment. Surface Sci 1993;281:153–62.

[124] Halperin WP. Quantum size effects in metal particles. Rev Mod Phys 1986;58:533–605.

[125] Kawabata A, Kubo R. Electronic properties of fine metallic particles. II. Plasma resonance absorption. J Phys Soc Jpn 1966;21:1765–72.

[126] Weick G. Quantum dissipation and decoherence of collective excitations in metallic nanoparticles. PhD thesis, Universite Louis Pasteur, Strasbourg and Universitat Augsburg, 2006.

[127] Prodan E, Nordlander P. Electronic structure and polarizability of metallic nanoshells. Chem Phys Lett 2002;352:140–6.

[128] Bruzzone S, Arrighini GP, Guidotti C. Some spectroscopic proper-ties of gold nanorods according to a schematic quantum model founded on the dielectric behavior of the electron-gas confined in a box. Chem Phys 2003;291:125–40.

[129] Prodan E, Radloff C, Halas NJ, Nordlander P. A hybridization model for the plasmon response of complex nanostructures. Science 2003;302:419–22.

[130] Wang H, Brandl DW, Nordlander P, Halas NJ. Plasmonic nanostructures: artificial molecules. Acc Chem Res 2007;40:53–62.

[131] Garcıa de Abajo FJ. Nonlocal effects in the plasmons of strongly interacting nanoparticles, dimers, and waveguides. J Phys Chem C 2008;112:17983–7.

[132] Mermin ND. Lindhard dielectric function in the relaxation-time approximation. Phys Rev B 1970;1:2362–3.

[133] Zheng J, Zhang C, Dickson RM. Highly fluorescent, water-soluble, size-tunable gold quantum dots. Phys Rev Lett 2004;93:077402.

[134] Patel SA, Richards CI, Hsiang J-C, Dickson RM. Water-soluble Ag nanoclusters exhibit strong two-photon-induced fluorescence. J Am Chem Soc 2008;130:11602–3.

[135] Khlebtsov BN, Khlebtsov NG. Biosensing potential of silica/gold nanoshells: sensitivity of plasmon resonance to the local dielectric environment. J Quant Spectr Radiat Transfer 2007;106:154–69.

[136] Lakhtakia A. Strong and weak forms of the method of moments and the coupled dipole method for scattering of time-harmonic electromagnetic fields. Int J Mod Phys 1992;3:583–603.

[137] Kolwas K, Demianiuk S, Kolwas M. Optical excitation of radius-dependent plasmon resonances in large metal clusters. J Phys B 1996;29:4761–70.

[138] Noguez CJ. Surface plasmons on metal nanoparticles: the influence of shape and physical environment. J Phys Chem C 2007;111:3806–19.

[139] Khlebtsov BN, Melnikov AG, Zharov VP, Khlebtsov NG. Absorption and scattering of light by a dimer of metal nanospheres: comparison of dipole and multipole approaches. Nanotechnology 2006;17:1437–45.

[140] Khlebtsov BN, Zharov VP, Melnikov AG, Tuchin VV, Khlebtsov NG. Optical amplification of photothermal therapy with gold nanoparticles and nanoclusters. Nanotechnology 2006;17:5167–79.

[141] Haiss W, Thanh NTK, Aveard J, Fernig DG. Determination of size and concentration of gold nanoparticles from UV–VIS spectra. Anal Chem 2007;79:4215–21.

[142] Khlebtsov NG. Determination of size and concentration of gold nanoparticles from extinction spectra. Anal Chem 2008;80:6620–5.

[143] Sancho-Parramon J. Surface plasmon resonance broadening of metallic particles in the quasi-static approximation: a numerical study of size confinement and interparticle interaction effects. Nanotechnology 2009;20:235706.

[144] Khlebtsov NG, Melnikov AG, Bogatyrev VA, Dykman LA, Alekseeva AV, Trachuk LA, et al. Can the light scattering depolarization ratio of small particles be greater than 1/3? J Phys Chem B 2005;109:13578–84.

[145] Brioude A, Jiang XC, Pileni MP. Optical properties of gold nanorods: DDA simulations supported by experiments. J Phys Chem B 2005;109:13138–42.

[146] Khlebtsov BN, Khlebtsov NG. Multipole plasmons in metal nanorods: scaling properties and dependence on the particle size, shape, orientation, and dielectric environment. J Phys Chem C 2007;111:11516–27.

[147] Bryant GW, García de Abajo FJ, Aizpurua J. Mapping the plasmon resonances of metallic nanoantennas. Nano Lett 2008;8:631–6.

[148] Prescott SW, Mulvaney P. Gold nanorod extinction spectra. J Appl Phys 2006;99:123504.

[149] Khlebtsov BN, Khanadeev VA, Khlebtsov NG. Observation of extra-high depolarized light scattering spectra from gold nanorods. J Phys Chem C 2008;112:12760–8.

[150] Calander N, Gryczynski I, Gryczynski Z. Interference of surface plasmon resonances causes enhanced depolarized light scattering from metal nanoparicles. Chem Phys Lett 2007;434:326–30.

[151] Laurent G, Felidj N, Aubard J, Levi G, Krenn JR, Hohenau A, et al. Evidence of multipolar excitations in surface enhanced Raman scattering. J Chem Phys 2005;122:011102.

[152] Payne EK, Shuford KL, Park S, Schatz GC, Mirkin CA. Multipole plasmon resonances in gold nanorods. J Phys Chem B 2006;110:2150–4.

[153] Kim S, Kim SK, Park S. Bimetallic gold–silver nanorods produce multiple surface plasmon bands. J Am Chem Soc 2009;131:8380–1.

[154] Schider G, Krenn JR, Hohenau A, Ditlbacher H, Leitner A, Aussenegg FR, et al. Plasmon dispersion relation of Au and Ag nanowires. Phys Rev B 2003;68:155427.

[155] Khlebtsov NG, Melnikov AG, Dykman LA, Bogatyrev VA. Optical properties and biomedical applications of nanostructures based on gold and silver bioconjugates. In: Videen G, Yatskiv YS, Mishchenko MI, editors. Photopolarimetry in remote sensing. Dordrecht: Kluwer Academic Publishers; 2004. p. 265–308.

[156] Markel VA. Divergence of dipole sums and the nature of non-Lorentzian exponentially narrow resonances in one-dimensional periodic arrays of nanospheres. J Phys B 2005;8:L115–21.

[157] Lamprecht B, Schider G, Lechner RT, Ditlbacher H, Krenn JR, Leitner A, et al. Metal nanoparticle gratings: influence of dipolar particle interaction on the plasmon resonance. Phys Rev Lett 2000;84:4721–4.

[158] Zhao LL, Kelly KL, Schatz GC. The extinction spectra of silver nanoparticle arrays: influence of array structure on plasmon resonance wavelength and widths. J Phys Chem B 2003;107:7343–50.

[159] Chumanov G, Sokolov K, Cotton TM. Unusual extinction spectra of nanometer-sized silver particles arranged in two-dimensional array. J Phys Chem 1999;100:5166–8.

[160] Malynych S, Chumanov G. Light-induced coherent interactions between silver nanoparticles in two-dimensional arrays. J Am Chem Soc 2003;125:2896–8.

[161] Khlebtsov BN, Khanadeyev VA, Ye J, Mackowski DW, Borghs G, Khlebtsov NG. Coupled plasmon resonances in monolayers of metal nanoparticles and nanoshells. Phys Rev B 2008;77:035440.

[162] Härtling T, Alaverdyan Y, Hille A, Wenzel MT, Käll M, Eng LM. Optically controlled interparticle distance tuning and welding of single gold nanoparticle pairs by photochemical metal deposition. Opt Express 2008;16:12362–71.

[163] Chen MW, Chau Y-F, Tsai DP. Three-dimensional analysis of scattering field interactions and surface plasmon resonance in coupled silver nanospheres. Plasmonics 2008;3:157–64.

[164] Davis TJ, Vernon KC, Gómez DE. Designing plasmonic systems using optical coupling between nanoparticles. Phys Rev B 2009;79:155423.

[165] Wurtz GA, Dickson W, O'Connor D, Atkinson R, Hendren W, Evans P, et al. Guided plasmonic modes in nanorod assemblies: strong electromagnetic coupling regime. Opt Express 2008;16:7460–70.

[166] Rong G, Wang H, Skewis LR, Reinhard BM. Resolving sub-diffraction limit encounters in nanoparticle tracking using live cell plasmon coupling microscopy. Nano Lett 2008;8:3386–93.

[167] Xu Y-l, Khlebtsov NG. Orientation-averaged cross sections of an aggregate of particles. J Quant Spectr Radiat Transfer 2003;78–80:1121–37.

[168] Su K-H, Wei Q-H, Zhang X, Mock JJ, Smith DR, Schultz S. Interparticle coupling effects on plasmon resonances of nanogold particles. Nano Lett 2003;3:1087–90.

[169] Lamprecht B, Leitner A, Aussenegg FR. SHG studies of plasmon dephasing in nanoparticles. Appl Phys B 1999;68:419–23.

[170] Mackowski D. Electrostatics analysis of radiative absorption by sphere clusters in the Rayleigh limit: application to soot particles. Appl Opt 1995;34:3535–45.

[171] Pinchuk AO, Schatz GC. Collective surface plasmon resonance coupling in silver nanoshell arrays. Appl Phys B 2008;93:31–8.

[172] Khlebtsov NG. Optical models for conjugates of gold and silver nanoparticles with biomacromolecules. JQSRT 2004;89:143–52.

[173] Reinhard MB, Siu M, Agarwal H, Alivisatos AP, Liphardt J. Calibration of dynamic molecular rulers based on plasmon coupling between gold nanoparticles. Nano Lett 2005;5:2246–52.

[174] Wei QH, Su KH, Durant S, Zhang X. Plasmon resonance of finite one-dimensional Au nanoparticle chains. Nano Lett 2004;4:1067–71.

[175] Jain PK, El-Sayed MA. Surface plasmon coupling and its universal size scaling in metal nanostructures of complex geometry: elongated particle pairs and nanosphere trimers. J Phys Chem C 2008;112:4954–60.

[176] Funston AM, Novo C, Davis TJ, Mulvaney P. Plasmon coupling of gold nanorods at short distances and in different geometries. Nano Lett 2009;9:1651–8.

[177] Aizpurua J, Bryant GW, Richter LJ, García de Abajo FJ. Optical properties of coupled metallic nanorods for field-enhanced spectroscopy. Phys Rev B 2005;71:235420.

[178] Mirkin CA, Letsinger RL, Mucic RC, Storhoff JJ. A DNA-based method for rationally assembling nanoparticles into macroscopic materials. Nature 1996;382:607–9.

[179] Faulk W, Taylor G. An immunocolloid method for the electron microscope. Immunochemistry 1971;8:1081–3.

[180] Krpetić Ž, Nativo P, Porta F, Brust M. A multidentate peptide for stabilization and facile bioconjugation of gold nanoparticles. Bioconjugate Chem 2009;20:619–24.

[181] Ojeda R, de Paz JL, Barrientos AG, Martín-Lomas M, Penadés S. Preparation of multifunctional glyconanoparticles as a platform for potential carbohydrate-based anticancer vaccines. Carbohydr Res 2007;342:448–59.

[182] Hermanson GT. Bioconjugate techniques. San Diego: Academic Press; 1996.

[183] Lowe CR. Nanobiotechnology: the fabrication and applications of chemical and biological nanostructures. Curr Opin Struct Biol 2000;10:428–34.

[184] Kong X-L, Qiao F-Y, Qi H, Li F-R. One-step preparation of antibody and oligonucleotide duallabeled gold nanoparticle bio-probes and their properties. Biotechnol Lett 2008;30:2071–7.

[185] Duchesne L, Gentili D, Comes-Franchini M, Fernig DG. Robust ligand shells for biological applications of gold nanoparticles. Langmuir 2008;24:13572–80.

[186] Liao H, Hafner JH. Gold nanorod bioconjugates. Chem Mater 2005;17:4636–41.

[187] Leonov AP, Zheng J, Clogston JD, Stern ST, Patri AK, Wei A. Detoxification of gold nanorods by treatment with polystyrenesulfonate. ACS NANO 2008;2:2481–8.

[188] Thierry B, Ng J, Krieg T, Griesser HJ. A robust procedure for the functionalization of gold nanorods and noble metal nanoparticles. Chem Commun 2009:1724–6.

[189] Wang C, Irudayaraj J. Gold nanorod probes for the detection of multiple pathogens. Small 2008;4:2204–8.

[190] Claridge SA, Mastroianni AJ, Au YB, Liang HW, Micheel CM, Fréchet JMJ, et al. Enzymatic ligation creates discrete multinanoparticle building blocks for self-assembly. J Am Chem Soc 2008;130:9598–605.

[191] Schrand AM, Braydich-Stolle LK, Schlager JJ, Dai L, Hussain SM. Can silver nanoparticles be useful as potential biological labels? Nanotechnology 2008;19:235104.

[192] Huang T, Nallathamby PD, Gillet D, Xu X-HN. Design and synthesis of single-nanoparticle optical biosensors for imaging and characterization of single receptor molecules on single living cells. Anal Chem 2007;79:7708–18.

[193] Stoscheck CM. Protein assay sensitive at nanogram levels. Anal Biochem 1987;160:301–5.

[194] Dykman LA, Bogatyrev VA, Khlebtsov BN, Khlebtsov NG. A protein assay based on colloidal gold conjugates with trypsin. Anal Biochem 2005;341:16–21.

[195] Leuvering JHW, Thal PJHM, van der Waart M, Schuurs AHWM. Sol particle immunoassay (SPIA). J Immunoassay 1980;1:77–91.

[196] Leuvering JHW, Thal PJHM, Schuurs AHWM. Optimization of a sandwich sol particle immunoassay for human chorionic gonadotrophin. J Immunol Meth 1983;62:175–84.

[197] Thanh NTK, Rosenzweig Z. Development of an aggregation-based immunoassay for anti-protein A using gold nanoparticles. Anal Chem 2002;74:1624–8.

[198] Englebienne P, van Hoonacker A, Verhas M, Khlebtsov NG. Advances in high-throughput screening: biomolecular interaction monitoring in real-time with colloidal metal nanoparticles. Comb Chem High Throughput Screen 2003;6:777–87.

[199] Ogawa A, Maeda M. Simple and rapid colorimetric detection of cofactors of aptazymes using noncrosslinking gold nanoparticle aggregation. Bioorg Med Chem Lett 2008;18:6517–20.

[200] Li H, Nelson E, Pentland A, Van Buskirk J, Rothberg L. Assays based on differential adsorption of single-stranded and double-stranded DNA on unfunctionalized gold nanoparticles in a colloidal suspension. Plasmonics 2007;2:165–71.

[201] Nam J-M, Thaxton CS, Mirkin CA. Nanoparticle-based bio-bar codes for the ultrasensitive detection of proteins. Science 2003;301:1884–6.

[202] Khlebtsov NG, Bogatyrev VA, Melnikov AG, Dykman LA, Khlebtsov BN, Krasnov YM. Differential light-scattering spectroscopy: a new approach to studying of colloidal gold nanosensors. JQSRT 2004;89:133–42.

[203] Roll D, Malicka J, Gryczynski I, Gryczynski Z, Lakowicz JR. Metallic colloid wavelength-ratiometric scattering sensors. Anal Chem 2003;75:3440–5.

[204] Pasternack RF, Collings PJ. Resonance light scattering: a new technique for studying chromophore aggregation. Science 1995;269:935–9.

[205] Liu X, Yuan H, Pang D, Cai R. Resonance light scattering spectroscopy study of interaction between gold colloid and thiamazole and its analytical application. Spectrochim Acta (Part A) 2004;60:385–9.

[206] Liu SP, He YQ, Liu ZF, Kong L, Lu QM. Resonance Rayleight scattering spectral method for the determination of raloxifene using gold nanoparticle as a probe. Anal Chim Acta 2007;598:304–11.

[207] Triulzi RC, Micic M, Orbulescu J, Giordani S, Mueller B, Leblanc RM. Antibody–gold quantum dot–PAMAM dendrimer complex as an immunoglobulin immunoassay. Analyst 2008;133:667–72.

[208] Butler JE, editor. Immunochemistry of solid-phase immunoassay. Boca Raton: CRC Press; 1991.

[209] Santos NC, Castanho MARB. An overview of the biophysical applications of atomic force microscopy. Biophys Chem 2004;107:133–49.

[210] Blab GA, Cognet L, Berciaud S, Alexandre I, Husar D, Remacle J, et al. Optical readout of gold nanoparticle-based DNA microarrays with silver enhancement. Biophys J 2006;90:L13–5.

[211] Raschke G, Kowarik S, Franzl T, Sönnichsen C, Klar TA, Feldmann J, et al. Biomolecular recognition based on single gold nanoparticle light scattering. Nano Lett 2003;3:935–8.

[212] Furuya T, Ikemoto K, Kawauchi S, Oga A, Tsunoda S, Hirano T, et al. A novel technology allowing immunohistochemical staining of a tissue section with 50 different antibodies in a single experiment. J Histochem Cytochem 2004;52:205–10.

[213] Duan L, Wang Y, Li SS, Wan Z, Zhai J. Rapid and simultaneous detection of human hepatitis B virus and hepatitis C virus antibodies based on a protein chip assay using nano-gold immunological amplification and silver staining method. BMC Infectious Diseases 2005; 5: 〈http://www.biomedcentral.com/1471-2334/5/53〉.

[214] Katz E, Willner I. Integrated nanoparticle–biomolecule hybrid systems: synthesis, properties, and applications. Angew Chem Int Ed 2004;43:6042–108.

[215] Brada D, Roth J. "Golden blot"-detection of polyclonal and monoclonal antibodies bound to antigens on nitrocellulose by protein A—gold complexes. Anal Biochem 1984;142:79–83;
Moeremans M, Daneles G, van Dijck A, Langanger G, de Mey J. Sensitive visualization of antigen–antibody reactions in dot and blot immune overlay assays with immunogold and immunogold/silver staining. J Immunol Meth 1984;74:353–60;
Surek B, Latzko E. Visualization of antigenic proteins blotted onto nitrocellulose using the immuno-gold-staining (IGS)-method. Biochem Biophys Res Commun 1984;121:284–9;
Hsu Y-H. Immunogold for detection of antigen on nitrocellulose paper. Anal Biochem 1984;142:221–5.

[216] Liang RQ, Tan CY, Ruan RC. Colorimetric detection of protein microarrays based on nanogold probe coupled with silver enhancement. J Immunol Meth 2004;285:157–63.

[217] Hou S-Y, Chen H-K, Cheng H-C, Huang C-Y. Development of zeptomolar and attomolar detection sensitivity of biotin-peptide using a dot-blot goldnanoparticle immunoassay. Anal Chem 2007;79:980–5.

[218] Cao C, Sim SJ. Signal enhancement of surface plasmon resonance immunoassay using enzyme precipitation-functionalized gold nanoparticles: a femto molar level measurement of anti-glutamic acid decarboxylase antibody. Biosens Bioelectron 2007;22:1874–80.

[219] Han S-M, Cho J-H, Cho I-H, Paek E-H, Oh H-B, Kim B-S, et al. Plastic enzyme-linked immunosorbent assays (ELISA)-on-a-chip biosensor for botulinum neurotoxin A. Anal Chim Acta 2007;587:1–8.

[220] Koo HC, Park YH, Ahn J, Waters WR, Palmer MV, Hamilton MJ, et al. Use of rMPB70 protein and ESAT-6 peptide as antigens for comparison of the enzyme-linked immunosorbent, immunochromatographic, and latex bead agglutination assays for serodiagnosis of bovine tuberculosis. J Clin Microbiol 2005;43:4498–506.

[221] Peng Z, Chen Z, Jiang J, Zhang X, Shen G, Yu R. A novel immunoassay based on the dissociation of immunocomplex and fluorescence quenching by gold nanoparticles. Anal Chim Acta 2007;583:40–4.

[222] Zhang S-B, Wu Z-S, Guo M-M, Shen G-L, Yu R-Q. A novel immunoassay strategy based on combination of chitosan and a gold nanoparticle label. Talanta 2007;71:1530–5.

[223] Zhang H, Meyerhoff ME. Gold-coated magnetic particles for solid-phase immunoassays: enhancing immobilized antibody binding efficiency and analytical performance. Anal Chem 2006;78:609–16.

[224] Khlebtsov BN, Dykman LA, Bogatyrev VA, Zharov VP, Khlebtsov NG. A solid-phase dot assay using silica/gold nanoshells. Nanosc Res Lett 2007;2:6–11.

[225] Khlebtsov BN, Khlebtsov NG. Enhanced solid-phase immunoassay using gold nanoshells: effect of nanoparticle optical properties. Nanotechnology 2008;19:435703.

[226] Malinsky MD, Kelly KL, Schatz GC, Van Duyne RP. Chain length dependence and sensing capabilities of the localized surface plasmon resonance of silver nanoparticles chemically modified with alkanethiol self-assembled monolayers. J Am Chem Soc 2001;123:1471–82.

[227] Khlebtsov NG, Bogatyrev VA, Dykman LA, Khlebtsov BN, Englebienne P. A multilayer model for gold nanoparticle bioconjugates: application to study of gelatin and human IgG adsorption using extinction and light scattering spectra and the dynamic light scattering method. Colloid J 2003;65:622–35.

[228] Khlebtsov NG, Trachuk LA, Melnikov AG. The effect of the size, shape, and structure of metal nanoparticles on the dependence of their optical properties on the refractive index of a disperse medium. Opt Spectrosc 2005;98:83–90.

[229] Miller MM, Lazarides AA. Sensitivity of metal nanoparticle surface plasmon resonance to the dielectric environment. J Phys Chem B 2005;109:21556–65.

[230] Chen H, Kou X, Yang Z, Ni W, Wang J. Shape- and size-dependent refractive index sensitivity of gold nanoparticles. Langmuir 2008;24:5233–7.

[231] Nusz GJ, Curry AC, Marinakos SM, Wax A, Chilkoti A. Rational selection of gold nanorod geometry for label-free plasmonic biosensors. ACS NANO 2009;3:795–806.

[232] Baciu CL, Becker J, Janshoff A, Sönnichsen C. Protein–membrane interaction probed by single plasmonic nanoparticles. Nano Lett 2008;8:1724–8.

[233] Wang Z, Ma L. Gold nanoparticle probes. Coord Chem Rev 2009;253:1607–18.

[234] Schultz DA. Plasmon resonant particles for biological detection. Curr Opin Biotechnol 2003;14:13–22.

[235] El-Sayed IH, Huang X, El-Sayed MA. Surface plasmon resonance scattering and absorption of anti-EGFR antibody conjugated gold nanoparticles in cancer diagnostics: applications in oral cancer. Nano Lett 2005;5:829–34.

[236] Huang X, El-Sayed IH, Qian W, El-Sayed MA. Cancer cell imaging and photothermal therapy in the near-infrared region by using gold nanorods. J Am Chem Soc 2006;128:2115–20.

[237] Loo C, Hirsch L, Lee M, Chang E, West J, Halas N, et al. Gold nanoshell bioconjugates for molecular imaging in living cells. Opt Lett 2005;30:1012–4.

[238] Hu R, Yong K-T, Roy I, Ding H, He S, Prasad PN. Metallic nanostructures as localized plasmon resonance enhanced scattering probes for multiplex dark-field targeted imaging of cancer cells. J Phys Chem C 2009;113:2676–84.

[239] Yang J, Eom K, Lim E-K, Park J, Kang Y, Yoon DS, et al. *In situ* detection of live cancer cells by using bioprobes based on Au nanoparticles. Langmuir 2008;24:12112–5.

[240] Eck W, Craig G, Sigdel A, Ritter G, Old LJ, Tang L, et al. PEGylated gold nanoparticles conjugated to monoclonal f19 antibodies as targeted labeling agents for human pancreatic carcinoma tissue. ACS NANO 2008;2:2263–72.

[241] Liopo AV, Copland JA, Oraevsky AA, Motamedi M. Engineering of hetero-functional gold nanorods for the *in vivo* molecular targeting of breast cancer cells. Nano Lett 2009;9:287–91.

[242] Wang B, Yantsen E, Larson T, Karpiouk AB, Su JL, Sokolov K, et al. Plasmonic intravascular photoacoustic imaging for detection of macrophages in atherosclerotic plaques. Nano Lett 2009;9:2212–7.

[243] Durr NJ, Larson T, Smith DK, Korgel BA, Sokolov K, Ben-Yakar A. Two-photon luminescence imaging of cancer cells using molecularly targeted gold nanorods. Nano Lett 2007;7:941–5.

[244] Sokolov K, Follen M, Aaron J, Pavlova I, Malpica A, Lotan R, Richards-Kortum R. Real-time vital optical imaging of precancer using anti-epidermal growth factor receptor antibodies conjugated to gold nanoparticles. Cancer Res 2003;63:1999–2004.

[245] Pieczonka NPW, Aroca RF. Single molecule analysis by surfaced-enhanced Raman scattering. Chem Soc Rev 2008;37:946–54.

[246] Kneipp J, Kneipp H, Kneipp K. SERS—a single-molecule and nanoscale tool for bioanalytics. Chem Soc Rev 2008;37:1052–60.

[247] Qian X-M, Nie SM. Single-molecule and single-nanoparticle SERS: from fundamental mechanisms to biomedical applications. Chem Soc Rev 2008;37:912–20.

[248] Kamnev AA, Dykman LA, Tarantilis PA, Polissiou MG. Spectroimmunochemistry using colloidal gold bioconjugates. Biosci Rep 2002;22:541–7.

[249] Chithrani BD, Ghazani AA, Chan WCW. Determining the size and shape dependence of gold nanoparticle uptake into mammalian cells. Nano Lett 2006;6:662–8.

[250] Jiang W, Kim BYS, Rutka JT, Chan WCW. Nanoparticle-mediated cellular response is size-dependent. Nat Nanotechnol 2008;3:145–50.

[251] Zhang G, Yang Z, Lu W, Zhang R, Huang Q, Tian M, et al. Influence of anchoring ligands and particle size on the colloidal stability and *in vivo* biodistribution of polyethylene glycol-coated gold nanoparticles in tumor-xenografted mice. Biomaterials 2009;30:1928–36.

[252] Parab HJ, Chen HM, Lai T-C, Huang JH, Chen PH, Liu R-S, et al. Biosensing, cytotoxicity, and cellular uptake studies of surface-modified gold nanorods. J Phys Chem C 2009;113:7574–8.

[253] Nativo P, Prior IA, Brust M. Uptake and intracellular fate of surface-modified gold nanoparticles. ACS NANO 2008;2:1639–44.

[254] Hauck TS, Ghazani AA, Chan WCW. Assessing the effect of surface chemistry on gold nanorod uptake, toxicity, and gene expression in mammalian cells. Small 2008;4:153–9.

[255] Mandal D, Maran A, Yaszemski MJ, Bolander ME, Sarkar G. Cellular uptake of gold nanoparticles directly cross-linked with carrier peptides by osteosarcoma cells. J Mater Sci: Mater Med 2009;20:347–50.

[256] Azzam EMS, Morsy SMI. Enhancement of the antitumour activity for the synthesised dodecylcysteine surfactant using gold nanoparticles. J Surfact Deterg 2008;11:195–9.

[257] Giljohann DA, Seferos DS, Patel PC, Millstone JE, Rosi NL, Mirkin CA. Oligonucleotide loading determines cellular uptake of DNA-modified gold nanoparticles. Nano Lett 2007;7:3818–21.

[258] Yang PH, Sun XS, Chiu JF, Sun HZ, He QY. Transferrin-mediated gold nanoparticle cellular uptake. Bioconjugate Chem 2005;16:494–6.

[259] Donnelly JJ, Wahren B, Liu MA. DNA vaccines: progress and challenges. J Immunol 2005;175:633–9.

[260] Dykman LA, Sumaroka MV, Staroverov SA, Zaitseva IS, Bogatyrev VA. Immunogenic properties of colloidal gold. Biol Bull 2004;31:75–9.

[261] Sadauskas E, Wallin H, Stoltenberg M, Vogel U, Doering P, Larsen A, Danscher G. Kupffer cells are central in the removal of nanoparticles from the organism. Part Fibre Toxicol 2007; 4: ⟨http://www.particleandfibretoxicology.com/content/4/1/10⟩.

[262] Shukla R, Bansal V, Chaudhari M, Basu A, Bhonde RR, Sastry M. Biocompartibility of gold nanoparticles and their endocytotic fate inside the cellular compartment: a microscopic overview. Langmuir 2005;21:10644–54.

[263] Vallhov H, Qin J, Johansson SM, Ahlborg N, Muhammed MA, Scheynius A, et al. The importance of an endotoxin-free environment during the production of nanoparticles used in medical applications. Nano Lett 2006;6:1682–6.

[264] Hillyer JF, Albrecht RM. Gastrointestinal persorption and tissue distribution of differently sized colloidal gold nanoparticles. J Pharm Sci 2001;90:1927–36.

[265] Niidome T, Yamagata M, Okamoto Y, Akiyama Y, Takahishi H, Kawano T, et al. PEG-modified gold nanorods with a stealth character for *in vivo* application. J Control Release 2006;114:343–7.

[266] De Jong WH, Hagens WI, Krystek P, Burger MC, Sips AJAM, Geertsma RE. Particle size-dependent organ distribution of gold nanoparticles after intravenous administration. Biomaterials 2008;29:1912–9.

[267] Semmler-Behnke M, Kreyling WG, Lipka J, Fertsch S, Wenk A, Takenaka S, et al. Biodistribution of 1.4 and 18 nm gold particles in rats. Small 2008;4:2108–11.

[268] Kattumuri V, Katti K, Bhaskaran S, Boote EJ, Casteel SW, Fent GM, et al. Gum arabic as a phytochemical construct for the stabilization of gold nanoparticles: *in vivo* pharmacokinetics and X-ray-contrast-imaging studies. Small 2007;3:333–41.

[269] Kogan B, Andronova N, Khlebtsov N, Khlebtsov B, Rudoy V, Dement'eva O, et al. Pharmacokinetic study of PEGylated plasmon resonant gold nanoparticles in tumor-bearing mice. NSTI-Nanotech 2008;2:65–8.

[270] Terentyuk GS, Maslyakova GN, Suleymanova LV, Khlebtsov BN, Kogan BY, Akchurin GG, et al. Circulation and distribution of gold nanoparticles and induced alterations of tissue morphology at intravenous particle delivery. J Biophoton 2009;2:292–302.

[271] Wang S, Lu W, Tovmachenko O, Rai US, Yu H, Ray PC. Challenge in understanding size and shape dependent toxicity of gold nanomaterials in human skin keratinocytes. Chem Phys Lett 2008;463:145–9.

[272] Fan JH, Hung WI, Li WT, Yeh JM. Biocompatibility study of gold nanoparticles to human cells. ICBME Proc 2009;23:870–3.

[273] Murphy CJ, Gole AM, Stone JW, Sisco PN, Alkilany AM, Goldsmith EC, et al. Gold nanoparticles in biology: beyond toxicity to cellular imaging. Acc Chem Res 2008;41:1721–30.

[274] Bastús NG, Casals E, Vázquez-Campos S, Puntes V. Reactivity of engineered inorganic nanoparticles and carbon nanostructures in biological media. Nanotoxicology 2008;2:99–112.

[275] Lewinski N, Colvin V, Drezek R. Cytotoxicity of nanoparticles. Small 2008;4:26–49.

[276] Ghosh P, Han G, De M, Kim CK, Rotello VM. Gold nanoparticles in delivery applications. Adv Drug Deliv Rev 2008;60:1307–15.

[277] Paciotti GF, Kingston DGI, Tamarkin L. Colloidal gold nanoparticles: a novel nanoparticle platform for developing multifunctional tumor-targeted drug delivery vectors. Drug Dev Res 2006;67:47–54.

[278] Patra CR, Bhattacharya R, Wang E, Katarya A, Lau JS, Dutta S, et al. Targeted delivery of gemcitabine to pancreatic adenocarcinoma using cetuximab as a targeting agent. Cancer Res 2008;68:1970–8.

[279] Cheng Y, Samia AC, Meyers JD, Panagopoulos I, Fei B, Burda C. Highly efficient drug delivery with gold nanoparticle vectors for *in vivo* photodynamic therapy of cancer. J Am Chem Soc 2008;130:10643–7.

[280] Hirsch LR, Stafford RJ, Bankson JA, Sershen SR, Rivera B, Price RE, et al. Nanoshell-mediated near-infrared thermal therapy of tumors under magnetic resonance guidance. Proc Natl Acad Sci USA 2003;100:13549–54.

[281] Pitsillides CM, Joe EK, Wei X, Anderson RR, Lin CP. Selective cell targeting with light-absorbing microparticles and nanoparticles. Biophys J 2003;84:4023–32.

[282] Berlien H-P, Mueller GJ. Applied laser medicine. Berlin: Springer; 2003.

[283] Palpant B, Guillet Y, Rashidi-Huyeh M, Prot D. Gold nanoparticles assemblies: thermal behaviour under optical excitation. Gold Bull 2008;41:105–15.

[284] Terentyuk GS, Maslyakova GN, Suleymanova LV, Khlebtsov NG, Khlebtsov BN, Akchurin GG, et al. Laser induced tissue hyperthermia mediated by gold nanoparticles: towards cancer phototherapy. J Biomed Opt 2009;14:021016.

[285] Nykypanchuk D, Maye MM, van der Lelie D, Gang O. DNA-guided crystallization of colloidal nanoparticles. Nature 2008;451:549–52.

[286] Park SY, Lytton-Jean AK, Lee B, Weigand S, Schatz GC, Mirkin CA. DNA-programmable nanoparticle crystallization. Nature 2008;451:553–6.